Research Square

Preprints are preliminary reports that have not undergone peer review.
They should not be considered conclusive, used to inform clinical practice,
or referenced by the media as validated information.

CD83 is a Targetable Inflammatory Marker of KRAS Mutant Cells in Myeloid Malignancies

Amit Verma

amit.verma@einsteinmed.edu

Albert Einstein College of Medicine https://orcid.org/0000-0002-5408-1673

Leah Kravets

Department of Oncology, Blood Cancer Institute, Albert Einstein College of Medicine, Montefiore Medical Center

Mirca Saurty-Seerunghen

Weill Cornell Medicine

Divij Verma

Albert Einstein College of Medicine https://orcid.org/0000-0002-2214-9450

Srabani Sahu

Albert Einstein College of Medicine

Rahul Sanawar

Department of Oncology, Blood Cancer Institute, Albert Einstein College of Medicine, Montefiore Medical Center

Swathi-Rao Narayanagari

Albert Einstein College of Medicine, Department of Cell Biology

Shanisha Gordon

Albert Einstein College of Medicine

Jinghang Zhang

Albert Einstein College of Medicine

Rongbao Zhao

Department of Oncology, Blood Cancer Institute, Albert Einstein College of Medicine, Montefiore Medical Center

Milagros Carbajal

Albert Einstein College of Medicine

Srinivas Aluri

Albert Einstein College of Medicine

Ariel Fromowitz

Montefiore Einstein Comprehensive Cancer Center

Olivia Sakaguchi

Weill Cornell Medicine

Chi-Lam Poon
Weill Cornell Medicine
Ritesh Agarwal
Albert Einstein College of Medicine
Jingli Wang
Albert Einstein College of Medicine
Amittha Wickrema
University of Chicago
Hussein Abbas
MD Anderson Cancer Center https://orcid.org/0000-0003-2946-3562
Mendel Goldfinger
Albert Einstein College of Medicine
Aditi Shastri
Albert Einstein College of Medicine
Ulrich Steidl
Albert Einstein College of Medicine https://orcid.org/0000-0002-9458-1795
Lindsay LaFave
Albert Einstein College of Medicine https://orcid.org/0000-0002-5203-4961
Marina Konopleva
Albert Einstein College of Medicine https://orcid.org/0000-0002-9347-2212
Anna Nam
Weill Cornell Medicine https://orcid.org/0000-0003-4192-8916

Article

Keywords:

Posted Date: November 19th, 2026

DOI: https://doi.org/10.21203/rs.3.rs-11528826/v1

License: This work is licensed under a Creative Commons Attribution 4.0 International License.
Read Full License

Additional Declarations: Yes there is potential Competing Interest. A.V. has received research funding from BMS, Jannsen, MedPacto, Curis, Prelude, Halia and Ryvu, has received compensation as a scientific advisor to Stelexis Therapeutics, Halia, Calico and Aurigene, is on the DSMC for Ascentage and has equity ownership in Roshon, Stelexis and clinStreet.

CD83 is a Targetable Inflammatory Marker of KRAS Mutant Cells in Myeloid Malignancies

Leah Kravets[1,2#], Mirca S. Saurty-Seerunghen[3#], Divij Verma[4#], Srabani Sahu[1,2], Rahul Sanawar[1,2], Swathi-Rao Narayanagari[5], Shanisha Gordon-Mitchell[1,2], Jinghang Zhang[7], Rongbao Zhao[1,2,], Milagros Carbajal-Rivera[1,2], Srinivas Aluri[1,2], Ariel Fromowitz[8], Olivia Sakaguchi[3], Chi-Lam Poon[3], Ritesh Agarwal[1], Jingli Wang[3], Amittha Wickrema[9], Abbas Hussein[10], Mendel Goldfinger[1], Aditi Shastri[1], Ulrich Steidl[3], Lindsay LaFave[3], Marina Konopleva[1 *], Anna S. Nam[3,11,12, 13 *], Amit Verma[1,2 *]

[1] Department of Oncology, Blood Cancer Institute, Montefiore Einstein Comprehensive Cancer Center, Bronx, New York, NY, USA

[2] Department of Developmental and Molecular Biology, Albert Einstein College of Medicine, Bronx, New York, NY, USA

[3] Department of Pathology and Laboratory Medicine, Weill Cornell Medicine, New York, NY, USA

[4] Department of Pathology, Albert Einstein College of Medicine, Bronx, New York, NY, USA

[5]Department of Cell Biology, Albert Einstein College of Medicine, Bronx, New York, NY, USA

[6]Department of Microbiology and Immunology, Albert Einstein College of Medicine, Bronx, New York, USA

[7] Department of Microbiology and Immunology, Albert Einstein College of Medicine, Bronx, New York, USA

[8]University of Maryland, School of Medicine, Baltimore, Maryland, USA

[9]University of Chicago, Chicago, IL

[10] Department of Leukemia, Division of Cancer Medicine, MD Anderson Cancer Center, The University of Texas; Houston, Texas, USA

[11]Biochemistry, Structural Biology, Cell Biology, Developmental Biology and Molecular Biology Graduate Programs, Weill Cornell Medicine; New York, NY, USA

[12]Tri-Institutional Training Program in Computational Biology and Medicine, Memorial Sloan Kettering Cancer Center, Cornell University, Weill Cornell Medicine, New York, NY, USA
[13] Sandra and Edward Meyer Cancer Center, Weill Cornell Medicine, New York, NY, USA

[#] Authors contributed equally to the work.

[*]Correspondence to:
amit.verma@einsteinmed.edu
shn9035@med.cornell.edu
marina.konopleva@einsteinmed.edu

Conflicts of Interest:
A.S.N. receives research funding from PharmaEssentia, unrelated to this work. A.V. has received research funding from BMS, Jannsen, MedPacto, Curis, and Prelude; has received compensation as a scientific advisor to Stelexis Therapeutics, Calico, Acceleron Pharma, Aurigene, and Celgene; and has equity ownership in Roshon Therapeutics, Throws Exception, and Stelexis Therapeutics. A.S. has received honoraria from PeerView, ACHL, Great Debates, HemeOnc Pulse, and Geron; has received advisory board fees from Kymera Therapeutics, Geron, Ryvu Therapeutic; has received research funding from Kymera Therapeutics and Ryvu Therapeutics; and is Data Safety Monitoring Board Chair for Servier Pharmaceuticals. D.V. holds patent WO2020016346A1 - "Periostin compounds for the treatment of haematological complications." M.K is on the advisory board of AbbVie, Auxenion GmbH, Dark Blue Therapeutics, Legend, MEI Pharma, Menarini/Stemline Therapeutics, Novartis, and Syndax; is a consultant for AbbVie, Adaptive, AmMax, Curis, Janssen, Kyowa Kirin, Menarini/Stemline Therapeutics, Novartis, Sanofi Aventis, Servier, and Vincerx; and receives funding from AbbVie, Janssen, and Klondike Biopharma. U.S. has received grants from GlaxoSmithKline, Bayer Healthcare, Aileron Therapeutics and Novartis, and personal fees from GlaxoSmithKline, Bayer Healthcare, Celgene, Aileron Therapeutics, Stelexis Therapeutics, Pieris Pharmaceuticals, Trillium and Pfizer outside the submitted work. U.S. has equity ownership in and has served on the board of directors of Stelexis Therapeutics outside the submitted work. U.S. has equity ownership in Roshon Therapeutics outside the submitted work.

Abstract :
KRAS mutations are enriched in resistant myeloid neoplasms and are associated with poor prognosis. The lack of distinct surface markers makes it difficult to distinguish RAS-mutant leukemic stem and progenitor cells from normal counterparts and define their functional properties within mixed human bone marrow populations. Thus, Genotyping of Transcriptomes was performed across a spectrum of myeloid malignancies and showed that *KRAS* mutant cells formed a distinct inflammatory, stem/progenitor-like population characterized by CD83 overexpression. $CD83^{+}$ mutant cells displayed impaired differentiation, whereas CD83 blockade in a novel transplantable $Kras^{G12D}$ mouse model reduced leukemogenic potential and prolonged survival. Selective $KRAS^{G12D}$ inhibition in patient samples and *in vivo* promoted erythroid differentiation, reduced monocytosis and tumor burden, and reversed inflammatory cytokine production. The transplantable $Kras^{G12D}$ model recapitulated human disease, including extramedullary granulocytic tumors, and responded to treatment with a selective $KRAS^{G12D}$ inhibitor. These findings identify CD83 as a novel therapeutic target across $KRAS^{G12D}$-mutant myeloid neoplasms.

SIGNIFICANCE: We found that *KRAS* mutations are enriched in a $CD83^{+}$ inflamed, quiescent AML subpopulation which drives leukemogenesis in a novel $Kras^{G12D}$ *in vivo* model. $KRAS^{G12D}$ inhibition reduces myeloproliferation and inflammation in diverse patient samples while eliminating myeloid sarcoma formation *in vivo.*

INTRODUCTION

Myeloid neoplasms are characterized by a myeloid blast expansion and dysregulated hematopoietic differentiation that can result in cytopenias, a major source of morbidity and mortality (1–5). Myelodysplastic syndrome (MDS), acute myeloid leukemia (AML) and pre-malignant clonal hematopoiesis (CH) are all associated with myeloid differentiation bias and inflammation (6–19) but the underlying molecular pathways are not fully elucidated.

RAS mutations occur in 19% of all cancers and in up to 30% of myeloid malignancies (20–28). KRAS mutations, most frequent at codon 12, 13 and 61, result in *KRAS* GTPase favoring the "on" position (*KRAS*-GTP) and activating downstream signaling pathways such as MAP-Kinase pathways (29). Consequently, a hematopoietic progenitor cell that acquires a *KRAS* mutation as a secondary genetic event is hypothesized to serve as a cooperating occurrence driving progression in myeloid malignancies (30,31), although the exact pathogenic mechanisms have not been elucidated at the single cell level in primary patient samples.

RAS-mutant AML cases are more resistant to standard treatments such as BCL-2 mimetics, FLT3 inhibitors, and IDH inhibitors (32–35). Furthermore, *KRAS* mutations can transform MDS or chronic myelomonocytic leukemia to AML and are associated with worse prognosis and survival outcomes in AML (25,28,35–40). Moreover, the prevalence of *KRAS* mutations has been shown to be higher even in some newly diagnosed AML cohorts, further underscoring the need to understand RAS-mutant myeloid malignancies (19,21,28,41–43).

In this study, we deployed single cell analysis of transcriptome and mutations within the same thousands of cells to elucidate specific *KRAS*^{G12D}-driven pathways in myeloid malignancies. Our findings reveal that inflammatory pathways are driven by *KRAS*^{G12D} mutant cells. Strikingly, we identified the role of CD83 upregulation in *KRAS*^{G12D} cells in AML patient samples. We also developed a novel transplantable AdenoCre-lox *Kras*^{G12D} hematological malignancy mouse model, which replicates the human myelomonocytic, CD83^{+} inflammatory phenotype. Using this model, we demonstrate the applicability of specific inhibitors to *KRAS*^{G12D} AML and the role that CD83 plays in promoting leukemogenesis.

RESULTS

Genotyping of Transcriptomes shows that *KRAS* G12D cells are enriched in the myelo-monocytic lineage in clonal hematopoiesis

Clonal hematopoiesis is characterized by the presence of somatic mutations in hematopoietic cells and represents the earliest detectable condition that can progress to myeloid malignancies (44). To understand the impact of *KRAS*^{G12D} mutation on pre-neoplastic hematopoiesis, we obtained bone marrow mononuclear cells (BMC) from a CH patient with a high variant allele frequency of the mutation (VAF: 39%) and no other clinically validated driver mutations (**Supplementary Table 1**). This case provides a rare opportunity to examine primary cells at a high resolution and differentiate between phenotypically similar *KRAS* wildtype (WT)

and *KRAS* mutant (MUT) cells that are otherwise indistinguishable by traditional single cell RNA sequencing (scRNA-seq) methods.

We deployed Genotyping of Transcriptomes (GoT) (45) that co-captures the transcriptome and mutational status within the same thousands of individual cells (**Fig. 1A**, **Supplementary Fig. 1A**, methods). First, cell types were annotated based on transcriptional profiles (**Fig. 1B-C**), and *KRAS* mutational status was overlaid via shared cell barcodes (**Fig. 1D**). We identified an enrichment of *KRAS* MUT cells among myeloid cells (i.e. monocytes, plasmacytoid dendritic cells (pDCs) and erythrocytes), in contrast to lymphocytes (**Fig. 1E-F**, **Supplementary Fig. 1B**), suggesting that the mutation may induce or favor a myeloid cell differentiation bias. To investigate dysregulations induced by oncogenic KRAS signaling, we performed differential expression analysis between *KRAS* mutant and wildtype cells followed by pathway enrichment analysis. For most cell types, there was no significant transcriptional difference between $KRAS^{G12D}$ and *KRAS*-WT cells. However, *KRAS* MUT erythroid cells showed an upregulation of cell cycle genes, chromatin remodelers, and DNA repair genes, and a downregulation of interferon gamma response in contrast to their WT counterparts (**Supplementary Fig. 1C-D**, **Supplementary Table 2**). *KRAS* mutations drove transcriptional dysregulation selectively in erythroid cells, likely due to lower basal activity of non-mutant *KRAS* in these cells compared to other lineages, as evidenced by reduced *KRAS* expression in the non-mutated state (**Supplementary Fig. 1E**).

***KRAS* G12D mutant cells in AML are enriched in an inflamed CD83 positive subgroup**

Next, to examine the role of *KRAS* mutation in myeloid neoplasms, we performed GoT on three AML patient samples (**Fig. 2A, Supplementary Fig. 2A, Supplementary Table 1)**. Hematopoietic cell lineages, including malignant subgroups (AML groups), from each patient sample were assigned based on whole transcriptomic signatures **(Fig. 2B-C, Supplementary Fig.2B-C)**.

We observed differential expression of *RUNX1*, *ETV6*, *JARID2*, and *ZEB2* in AML cells compared to non-malignant cells, representing known leukemia pathways involved in driving disease and contributing to the leukemic cell pool (**Fig. 2D**). Interestingly, we also identified that inflammatory genes such as *CD83*, *NFKB1*, *NLRP3* and *TNFAIP8* were significantly upregulated in AML cells (**Supplementary Fig. 2D**). We observed AML cell state heterogeneity, including cell states driven by cell cycle activity or differentiation programs, as well as cell states less clearly defined (i.e. AML-GroupA, B or C, **Fig. 2B**, **Supplementary Fig. 2B**). One particular subset of AML cells, AML-GroupB, was characterized by significantly elevated *CD83*, *NFKB1*, *NLRP3*, *TNFAIP8*, *CHST11*, *IMMP2L*, *CDK6*, *RBM47* gene expression in comparison to other AML subgroups (**Fig. 2E, Supplementary Fig. 2E**).

To investigate whether the *KRAS* mutation drives inflammation in AML, we intersected the *KRAS* mutational status from GoT with the AML subgroups (**Fig. 2F**, **Supplementary Fig. 3A-C**). Indeed, we observed an enrichment of *KRAS* MUT cells among AML-GrpB cells (**Fig. 2G**, **Supplementary Fig. 3C-D**). Consistently, differential expression analysis between *KRAS* MUT and WT AML cells revealed an upregulation of inflammatory (e.g. *CD83*, *IL6*, *TLR3*,

IL10RA) and interferon genes in *KRAS* MUT cells (**Fig. 2H-I**, **Supplementary Table 3**). CD83, an immune response modulator (46–48), was significantly overexpressed in MUT AML cells in comparison to WT cells, specifically in MUT AML-GrpB, AML with monocytic differentiation, and cycling AML cell groups (**Fig. 2J**). We also observed an enrichment of CD83-expressing cells among *KRAS* MUT cells, CD83 as a marker of *KRAS*-mutant AML cells (**Fig. 2K**). Coherently, these groups also demonstrated an upregulation of module scores related to inflammation, including TNF signaling via NF-kB (MsigDB Hallmark; **Fig. 2L**, **Supplementary Fig. 3E**). These results support the model in which *KRAS*-mutant AML cells display an inflammatory phenotype.

Additionally, we observed a downregulation of cell cycle pathways in *KRAS* MUT AML cells (**Fig. 2I**, **Supplementary Table 3**), more specifically in the cycling and AML-GrpB cell groups (**Supplementary Fig. 3F**). This suggested that *KRAS* mutation may confer a less proliferative, more quiescent state to AML cells that has stem cell-like characteristics. To test this, we assessed whether quiescence genes were differentially expressed in AML cell subsets (49). We found that AML-GrpB cells expressed highest levels of quiescence genes compared to other AML subgroups (**Fig. 2M**) and that quiescence genes are upregulated in *KRAS* MUT cells (**Fig. 2N**).

CD83^{+} cells are enriched in CD34^{+} stem/progenitor population and produce decreased colony counts

To investigate the role of CD83 in myeloid neoplasms, we first assessed its gene expression in a larger and more diverse AML cohort. We used a gene expression data set comprised of sorted stem and progenitor cells of healthy controls (n=4-6) AML patients (n=12-18) with monosomy chr7 (-7), complex karyotype (CK), and normal karyotype (NK) (50). *CD83* expression was significantly enriched in long term HSCs, short term HSCs, and GMPs in AML cells (n=12-18) in comparison to healthy controls (HC; n= 4-6) (**Fig. 3A**, **Supplemental Fig. 4A**). Of note, NK AML had the most significant CD83 overexpression within each sorted cell grouping compared to CK and -7 AML (**Supplemental Fig. 4A**).

To explore the impact of CD83 on hematopoietic stem cell functionality, we sorted CD83^{+} and CD83^{-} PBMCs from a *KRAS*^{G12D} MDS patient (**Fig. 3B**, **Supplementary Fig. 4B**). Equal numbers of sorted cells were cultured in MethoCult for 2 weeks. Flow cytometry analysis on colonies showed a higher expression of CD34 among sorted CD83^{+} cells than among CD83^{-} sorted cells and unsorted cells (**Fig. 3C**, **Supplementary Fig. 4C**). Additionally, CD83^{+} cells led to decreased erythroid and myelomonocytic colony formation in comparison to CD83^{-} and unsorted cells (**Fig. 3D**, **Supplementary Fig. 4D**). These data suggest a more stem-like and quiescent state adopted by CD83^{+} cells from this *KRAS*^{G12D} MDS sample, consistent with the GoT analyses of primary AML cells (**Fig. 2M-N**, **Supplementary Fig. 3F**).

Specific inhibitor of KRAS G12D decreases frequency of mutant cells, myelo-monocytic bias and inflammation

To test whether the observed *KRAS*^{G12D} phenotype is reversible, we treated *KRAS*^{G12D} BMCs from a CH patient with a *KRAS*^{G12D}-specific inhibitor, MRTX1133, in MethoCult for 14

days. We deployed GoT on the treated cells to determine the impact of MRTX1133 on the differentiation and transcriptional states of isolated *KRAS*^{G12D} in human hematopoiesis (**Fig. 4A**, **Supplementary Fig. 5A**). Expected hematopoietic cell types from MethoCult were identified by cell clustering based on whole transcriptomes alone (**Fig. 4B**, **Supplementary Fig. 5B**). MRTX1133 treatment decreased the myeloid cell population, notably the granulocytic monocytic progenitors (GMPs) and monocytes (**Fig. 4C**). It also increased the erythrocyte population, especially evident in the proliferative subset (**Fig. 4C**). Remarkably, MRTX1133 treatment significantly reduced the *KRAS* mutant cell proportion and allowed for the relative expansion of WT cells ($P < 10^{-10}$, Fisher exact test, **Fig. 4D**, **Supplementary Fig. 5C**). Consistently, we observed a reduced expression of pro-inflammatory *S100A9* upon MRTX1133 treatment and significantly decreased the overall inflammatory gene score, especially in the monocytes (**Fig. 4E-F**). Inhibition of *KRAS* G12D reduced inflammatory genes including *CD83* and interferon genes, while increasing cell cycle pathways and heme metabolism in GMPs (**Fig. 4G-H, Supplementary Table 4**).

To validate these effects of specific *KRAS* G12D inhibition, we cultured the same mutant CH BMCs for two weeks in MethoCult and evaluated their differentiation markers using flow cytometry. Upon MRTX1133 treatment, we found a significant decrease in monocytes ($CD11b^{+}CD14^{++}$) and myelomonocytic colonies (**Fig. 5A-D**, **Supplementary Fig. 6A**). We observed a similar trend in a *KRAS*^{G12D} MDS patient and *KRAS*^{G12D} AML patient with KMT2A rearrangement (hereafter designated as MDS1 and AML4; **Fig. 5A-D**), as the inhibitor treatment decreased myeloid blasts and monocytes ($CD11b^{+}CD14^{++}$; **Fig. 5D**).

As the CH sample was enriched for KRAS-mutant erythroid cells (**Fig. 1E-1F)**, we could not evaluate WT erythroid colonies using our *in vitro* assays. Additionally, the AML4 sample produced only myelomonocytic colonies in culture (**Fig. 5B**). However, the MDS1 patient sample demonstrated a significantly increased erythroid compartment ($\%CD45^{-}$) and erythroid colonies, suggesting a relief in the differentiation block (**Supplementary Fig. 6B**). Lastly, to validate if inflammation decreases *in vitro* upon KRAS G12D inhibition, CH samples were treated with MRTX1133 resulting in a significant reduction of the proportion of inflammatory stem cells ($CD34^{+}CD83^{++}$) (**Fig. 5E-F**). To investigate whether MRTX1133 treatment is toxic to mononuclear cells, we treated PBMCs from healthy individuals and observed no toxicity of MRTX1133 treatment (**Supplementary Fig. 6C-D**). Altogether, these results demonstrated that specific inhibition decreases *KRAS* mutational burden along with the associated inflammation. MRTX1133 blocks myeloproliferation and relieves the erythroid differentiation block, with no toxicity to *KRAS* wildtype cells.

Establishing the transplantable *Kras*^{G12D} *in vivo* model

To study *Kras*^{G12D} driven myeloid malignancy *in vivo*, we developed a transplantable *Kras*^{G12D} model. Briefly, c-Kit^{+} bone marrow cells were isolated from a C57Bl6 mouse heterozygous for both *Kras*$^{LSL(lox\text{-}stop\text{-}lox)\text{-}G12D/+}$ and Rosa26-LSL-tdTomato to enrich for stem cells (**Fig. 6A**, **Supplementary Fig. 7A-B**). Cells were spinfected twice over two days using

Ad5CMVCre virus and transplanted into sub-lethally-irradiated C57Bl6 mice (**Fig. 6A**). Disease progression in mice following transplantation was assessed through hematoxylin and eosin (H&E) staining of tissues, which revealed an increasing number of infiltrating leukemic cells that progressively disrupted the normal structure of the liver and spleen over time (**Fig. 6B**). Necropsy of a mouse 4 months post-transplant demonstrated extramedullary hematopoiesis by its enlarged liver, enlarged spleen, and discolored kidneys (**Supplementary Fig. 7B)**. Moreover, older mice developed tumors in the thymic region, invading the ribcage and lungs, and attached to the spine (**Supplementary Fig. 7B**). Flow cytometry revealed that a large proportion of tdTomato^{+}, or *KRAS* mutant cells in the tumor mass, expressed CD34, with partial CD11b expression (**Fig. 6C**), suggestive of a myeloid sarcoma. It also revealed that BMCs of primary engrafted mice were engrafted with *Kras*$^{G12D+}$ cells, which displayed reduced Ter119^{+} and increased CD11b^{+} cells (**Fig. 6D**, **Supplementary Fig. 7C**).

To classify the type of myeloid malignancy exhibited in our transplantable model, we harvested bone marrow cells from a 4-month-old primary AdenoCre-Lox mouse for transplantation into secondary irradiated recipients (**Fig. 6E**). This donor mouse displayed extensive leukemic cell infiltration of the kidneys, spleen, liver, and thymic tumor as evidenced by organomegaly and H&E staining (**Supplementary Fig. 7D-F)**. Additional features include anemia (suggested by nearly white bone marrow), with a skeletal defect in the tibia in comparison to the irradiated WT control donor (**Supplementary Fig. 7E-F**). All recipients of bone marrow cells from AdenoCre-Lox (recipients abbreviated as Cre-lox) succumbed to lethal disease in less than 25 days, in comparison to the WT recipient controls (**Fig. 6E**). Hematological parameters demonstrate that Cre-lox mice exhibit significantly increased white blood cells (WBCs) and monocytes, while red blood cells (RBCs), hemoglobin (Hb), hematocrit (HCT), platelet count (PLT), plateletocrit (PCT), and neutrophils were significantly decreased compared to WT controls, suggesting myeloid disease accompanied by cytopenias (**Fig. 6F, Supplementary 8A).** Other hematological parameters show the recombinant *Kras* mutant cells differentiated into multiple lineages, as evidenced by significantly altered mean corpuscular volume (MCV), red cell distribution width (RDW), reticulocytes, and basophils in Cre-lox mice as compared with WT controls (**Supplementary Fig. 8A**). Flow cytometric analysis of Cre-lox bone marrow, peripheral blood, thymus, and spleen demonstrated that the *Kras*^{G12D} compartment was enriched for hematopoietic stem progenitor marker CD34 (**Fig. 6G-J**). Additionally, *Kras* MUT cell compartment of Cre-lox bone marrow and spleen demonstrated significant reductions in Ter119^{+} expression (**Fig. 6G**, **Fig. 6J**). Furthermore, Cre-lox mice demonstrate organomegaly, as evidenced by splenomegaly, hepatomegaly, and thymomegaly in (**Fig. 6K)**. H&E staining confirms organomegaly via infiltrating leukemic cells in bone marrow, liver, spleen, thymus, kidney, salivary glands, and pancreas, suggesting disseminated myeloid sarcomas (**Fig. 6L**, **Supplementary Fig. 8B**). Collectively, these findings support the interpretation that this model represents an aggressive leukemic process.

Next, we transplanted total bone marrow cells from a 2-month-old primary engrafted mouse into sublethally-irradiated C57Bl6 mice to test the impact of MRTX1133 treatment in a less

severe disease model (**Fig. 6M**). We found that mice secondarily engrafted with *Kras*^{G12D} BMCs also had significantly less erythrocytic Ter119^{+} cells in comparison to *Kras*^{WT} cells (**Fig. 6M**, **Supplementary Fig. 8C-8D**). Furthermore, *Kras*^{G12D} BMCs were enriched in CD83 Median Fluorescent Intensity (**Fig. 6M**). Collectively, these results show that our mouse model displays a myeloid bias, develops myeloid sarcomas, and overexpresses CD83 in *Kras*^{G12D} cells, mimicking AML in humans.

Kras G12D specific inhibitor eliminates tumor formation in secondarily engrafted mice

To investigate whether MRTX1133 eliminates *Kras*^{G12D}-mutant myeloid neoplasm *in vivo*, we separated secondarily transplanted mice into treatment and vehicle groups, equally distributing animals into two groups based on weight, sex, and percentage of *Kras*^{G12D} bone marrow engraftment (**Fig. 7A**). We administered 10 mg/kg of the drug or vehicle intraperitoneally to each group for the first three weeks of treatment (5 days per week). During the final week, mice received 10 mg/kg daily, with an additional 10 mg/kg dose given every other day. At experimental endpoint, five of the seven vehicle-treated mice developed tumors found in the thymic region, while none of the MRTX1133-treated mice did (**Fig. 7B**). Flow cytometry analysis showed that *Kras*$^{G12D+}$ cells constituted more than 90% of the tumor tissue (**Fig. 7C**). CD11b and CD34 expression were elevated in *Kras*^{G12D} cells, compared to *Kras*^{WT} cells (**Fig. 7C**). Furthermore, circulating cells from MRTX1133-treated mice showed a 24-fold reduction in *Kras*^{G12D} cells compared with control mice, almost eliminating the leukemic form of the neoplasm (**Fig. 7D**). Consistently, MRTX1133-treated mice exhibited fewer circulating *Kras*$^{G12D+}$CD34^{++} or mutant extramedullary leukemic cells (**Fig. 7D**). MRTX1133-treated PBMCs had significantly increased WT Ter119 expression and significantly decreased CD11b expression in *Kras*$^{G12D+}$ in comparison to vehicle treated, suggesting MRTX1133 decreases myelomonocytic differentiation, leukocytosis, and relieves the erythroid differentiation block (**Fig. 7D**, **Supplementary Fig. 9A**). Erythropoietic parameters like MCV and reticulocytes seen previously elevated in Cre-lox mice were significantly reduced in MRTX1133 treated mice, suggesting a decrease in ineffective erythropoiesis (**Supplementary Fig. 9B**). Additionally, mice treated with MRTX1133 exhibited a 40% reduction in splenic MUT cells, compared to vehicle-treated mice (**Fig. 7E**), demonstrating that MRTX1133 can reduce splenic tumor burden. This was further evidenced by the significant reduction in normalized spleen and liver weights in MRTX1133-treated mice compared to vehicle-treated mice (**Fig. 7F**). Moreover, H&E staining demonstrated that MRTX1133 reduced leukemic cell infiltration as seen by less leukemic cells in long bones, spleen, and liver (**Fig. 7G**). MRTX1133 treated mice have significantly less circulating CD83^{+}*Kras*$^{G12D++}$ cells (CD83^{+}Tdtomato^{++}) and circulating inflammatory stem cells (CD83^{+}CD34^{++}), further linking Kras mutations and CD83 driven inflammation in mice (**Fig. 7H**). Lastly, MRTX1133 treated mice had significantly elevated plasma IFN-α, while IL-6, IL-10, and TNF-α levels were decreased suggesting that Kras G12D specific inhibition broadly remodels the immune system (**Fig. 7I)**. Thus, MRTX1133 eliminated the formation of *Kras*$^{G12D+}$ myeloid sarcomas, leukemia, and inflammation in our transplantable

mouse model, providing a preclinical *in vivo* proof-of-principle data for *KRAS*^{G12D}-treatment for human AML.

CD83 Promotes Leukemogenesis *in vivo*

To investigate if blocking CD83-mediated pathways alters leukemogenesis in the AdenoCrelox mice, we treated primary engrafted mice with CD83 neutralizing antibody (nAb) or isotype control and subsequently transplanted treated bone marrow (**Fig. 8A**, **Supplementary Fig. 10A**). First, our newly generated cohort of primary engrafted mice were phenotypically steady due to consistently reduced erythroid differentiation and increased inflammation in mutant cells, as evidenced by significantly less Ter119 expression and significantly higher CD83 MFI in the *Kras*^{G12D} compartment as compared to the *Kras*^{WT} compartment (**Fig. 8B**, **Supplementary Fig. 10B**). After confirming that the anti-CD83 antibody binds to mouse CD83 ligand with high affinity, primary engrafted mice with similar *Kras*^{G12D} engraftment levels and proportion of CD83-expressing cells were assigned to receive anti-CD83 nAb antibody or isotype control (**Fig. 8C-D**). After primary mice were treated for two months, bone marrow cells were transplanted into secondary irradiated recipients. Recipients of anti-CD83 nAb treated bone marrow cells had significantly less *Kras*^{G12D} cell engraftment than isotype-control treated recipient mice (**Fig. 8E**). These findings correlated to probability of survival, as anti-CD83 nAb treated recipient mice had significantly longer survival than isotype-control treated recipient mice (**Fig. 8F**). This was true for transplantation of treated bone marrow, all which support a role of CD83 in leukemogenesis *in vivo* (**Fig. 8F**). Therefore, the effects of CD83 blockade suggest that CD83-driven pathways contribute to disease pathogenesis.

DISCUSSION

RAS-driven myeloid malignancies are associated with poor prognosis and outcomes (22,25,35–39). *KRAS* mutations are particularly enriched in leukemias that are resistant to standard-of-care treatments (32–35) which have remained largely unchanged over the past decade. Thus, elucidating the mechanisms by which *KRAS* mutations drive disease allows identification of clinically relevant markers for novel therapeutic development. Research on KRAS-driven myeloid neoplasms has been hampered by the lack of representative models. Additionally, conventional approaches, such as flow cytometry, are unable to distinguish the often subclonal *KRAS*-mutant leukemia cells from *KRAS*-wildtype cells in patient samples, further complicating research efforts. In this study, we leveraged GoT to overcome this limitation, enabling us to characterize the contribution of RAS mutant cells to carcinogenicity. Namely, our investigations revealed that *KRAS* mutations induce an erythroid differentiation block, monocytic differentiation bias, and inflammation in both patient samples and mouse studies. Additionally, our discovery of KRAS role in enhancing inflammation-associated quiescence in leukemia may underlie the therapy-resistance of *KRAS* MUT clones.

Our discovery that *KRAS* mutant cells are enriched in a novel stem progenitor like inflamed population, AML GrpB, is currently being explored in non-RAS mutant AML samples to validate whether AML GrpB represents a RAS driven subgroup. CD83 positivity marked this subgroup, a surface marker also upregulated in lymphoma, myeloma, myeloid malignancy cell lines, $CD34^+$ AML blasts (46–48,51–53), and is associated with an inflammatory transcriptome (54,55). CD83 behaves similarly in solid tumors, as a large single-cell transcriptomic study (378 solid tumors, 12 cancer types) found that $CD83^+$ tumor-associated neutrophils suppress anti-tumor cytotoxicity and correlate with poor patient prognosis and immunotherapy resistance (56). In-depth genetic interaction network studies found that $KRAS^{G13D}$ negatively interacts with CD83, such that simultaneously blocking KRAS whilst knocking down CD83 decreased colonic tumors by 50% *in vivo* (57). This interaction may involve NF-κB signaling, which is activated by mutant *KRAS* (58,59), and is a known transcriptional regulator of CD83 expression (60,61). Finally, CD83 CAR T therapy is currently being tested in a phase IB clinical trial to prevent AML graft-versus-host disease and relapse (52). This CAR T works *in vitro* by increasing interferon responses while decreasing IL-6, similarly to MRTX1133 treatment in our *in vivo* studies (53). If responses in CD83 CAR T-treated RAS mutant patients are positive, it will further support our hypothesis of targeting CD83 in myeloid malignancies.

Elevated expression of another inflammatory marker, *S100A8*, was observed in *KRAS* mutant monocytes, monocytic progenitors (MP), and immature/common myeloid progenitors (IMP/CMP) in the cultured CH patient sample. Additionally, its downregulation was observed in circulating plasma of MRTX1133 treated mice. Furthermore, all three AML patient samples displayed elevated *S100A9* expression in AML monocytes across all samples. S100A8/A9 is an inflammatory molecule highly upregulated in myeloid malignancies that induces myeloid-derived suppressor cell growth, resulting in an immunosuppressive environment that stifles T cell function and proliferation needed for malignant cell clearance (62,63). Once S100A8/A9 binds its cognitive receptor, the NLRP3 inflammasome is activated and induces cytokine secretion (63). GoT analysis identified the upregulation of the following inflammasome genes: *NFKB1* and *NLRP3* in mutant AML grpB cells and *IL1B* in untreated CH GMPs. Targeting these inflammatory pathways observed in the $KRAS^{G12D}$ mutant cells may be a potential therapeutic avenue for alleviating KRAS-driven myeloid disease. Consistently, a $KRAS^{G12D}$ chronic myelomonocytic leukemia patient with elevated *NLRP3* expression was treated with an IL-1 receptor blocker, resulting in reduced monocytic disease and improved patient's status to allow for a stem cell transplant (64). Therefore, targeting inflammatory pathways downstream of $KRAS^{G12D}$ signaling could reduce the inflammatory microenvironment that enables RAS mutant malignant cells to persist and proliferate.

Lastly, our *in vivo* model is the first isolated $Kras^{G12D}$ mutant mouse to develop a myeloid sarcoma, or extramedullary leukemia, that mimics human myeloid sarcomas, given its high composition of immature $CD34^+$ myeloid blasts (65,66). Other transplantable $Kras^{G12D}$ conditional

knock-in models developed an aggressive T cell disease with thymic enlargement or thymic tumor development (67,68), while other *Kras*^{G12D} models had a combination of myeloproliferative and lymphoma phenotypes (13,15,69,70). More comparable models skew myeloid (14,71) and describe a similar multilineage phenotype to ours (e.g. leukocytosis, ineffective erythropoiesis, cytopenia, and high reticulocytes) (12,13,15,17,71–74). Additionally, our observation of high circulating TNF-α in vehicle-treated *Kras*^{G12D} mice is corroborated by findings of high TNF-α in other *Kras*^{G12D} mouse bone marrow endothelial cells and progenitor cells *in vivo* (13,17). We hypothesize that our *Kras*^{G12D} driven leukemic model results from the ectopic non-physiological expression of *Kras*^{G12D} from the Rosa26 locus, especially because RAS mutations are secondary genetic events in human AML (11).

Our *in vivo* AdenoCre-Lox model is translatable to disease pathology in humans, as mutations in the RAS pathway are reported in 30-85% of myeloid sarcomas, with *KRAS* mutations accounting for up to 18% of cases (66,75–77). Generally, extramedullary leukemia develops in 9% of adult AML cases and 40% of pediatric AML patients (65). Additionally, our mouse model recapitulates the *KRAS*^{G12D} multilineage differentiation seen in both CH and AML patient samples, including ineffective erythropoiesis within the *KRAS*^{G12D} erythroid lineage. Finally, the reduction of circulating inflammatory cytokines observed in MRTX1133 treated mice is consistent with upregulated inflammatory genes and pathways in *KRAS*-mutant AML cells (CD83, IL-10RA, IL-6, TNF-α) and in *KRAS*^{G12D} CH cells (CD83, IL-6, TNF-α). Lastly, the AdenoCre-Lox mice encompass myelomonocytic disease accompanied by cytopenias, which is consistent with human disease, making this a relevant model for understanding CD83 driven inflammatory pathways and testing future therapeutics.

To our knowledge, no other study has examined the impact on the specific inhibition of *KRAS*^{G12D}-mutated AML. Additionally, it is likely that other RAS mutations and RAS pathway mutations in AML drive similar inflammatory programs, suggesting our study as a proof of concept for a broad range of RAS mutant myeloid malignancies. Lastly, our data provides evidence for therapeutic benefits of treating *KRAS*^{G12D}-mutated AML with KRAS-mutant specific inhibitors, especially those with relapse and therapy resistance, likely in combination with other immunotherapies.

METHODS:

Patient samples

Peripheral blood (PB) or bone marrow aspirate (BM) samples from AML patient samples were obtained from MD Anderson under sample collection protocol: LAB01-473 and local Einstein IRB protocol 2023-14731. PB and BM samples from MDS and Clonal Hematopoiesis (CH) patients were obtained from Montefiore Comprehensive Cancer Center using tissue collection (IRB protocol 2005-536).

Mononuclear cell isolation

Fresh PB or BM was mixed with 2x volume of IMDM (Cytiva, SH30228.FS). 20-30 mL of mixed blood was layered with 10 mL of Ficoll-Paque (Cytiva 45-001-751). Samples were spun for 45 minutes, 475 g (acceleration 9, deceleration 0). Cells were carefully extracted from the buffy coat layer and washed twice with 5 mL of complete IMDM media (400 g, 5-10 minutes) before cell culture or cryopreservation (media: 90% FBS, 10% DMSO) for freezing at -80 °C, and then moved into liquid nitrogen after 3 days.

$CD34^+$ cell isolation

For $CD34^+$ isolation from AML 3 patient BMCs, CD34 Microbead Kit UltraPure human product (130-100-453) protocol was used.

Clonogenic Assays for cell treatment with *KRAS* G12D-specific inhibitor

MRTX1133 was purchased from MedChemExpress (HY-134813), aliquoted at 1 mM, and frozen at -80 °C. Cryopreserved peripheral blood PB or BM were rapidly thawed in 37°C and then cells were added dropwise to 10 mL of cIMDM (10% FBS, 1% Pen/Strep) and then centrifuged at 350g, room temperature, for 5 minutes. 200,000-300,000 live cells from patient samples were prepared per condition in 300 uL of IMDM media with 10% FBS (Gemini Bio, 100-106) and 1% Pen/Strep (Gemini Bio, 400-109) with drug or DMSO (hereafter designated as MRTX1133 and Vehicle, respectively). Untreated samples (n=2) were prepared for single color controls. This was mixed into 3 mL of MethoCult medium (STEMCELL, H4435) and vortexed three times. Using a 3mL syringe with a 16 gauge blunt end needle (STEMCELL, 28810), half of the 3.3 mL mixture was distributed into 2 wells of a 6-well tissue culture plate. After 14 days of culture, 3 mL of PBS buffer was added to each well and incubated for 30 minutes at 37°C to dissolve the methocult. The following steps were done on ice: duplicate conditions were pooled and washed twice with 5 mL PBS for 15 minutes, 350g, 4 °C.

GoT Experiment

To simultaneously capture whole transcriptomic data and KRAS mutational status, Genotyping of Transcriptomes (GoT) was performed as previously described (45). Briefly, cryopreserved cells from peripheral blood or BM (from bone marrow aspirates) were thawed as per the "Thawing & Resuspension" portion of 10X Genomics Demonstrated Protocol CG00039, Rev D, "Fresh Frozen Human PBMCs for Single Cell RNA Sequencing." If cells were treated with MRTX1133, see "Clonogenic Assays for cell treatment with KRAS-G12D-specific inhibitor" for how cells were thawed, treated, and washed. The standard 10x Genomics Chromium 5′v.2 chemistry was implemented according to the manufacturer's recommendations up to the cDNA amplification step (10x Genomics, Pleasanton, CA). After cDNA amplification and SPRI bead (Beckman Coulter) cleanup, 10x scRNA-seq libraries were generated as recommended. To capture the KRAS genotype of each cell, 3 µL of the cDNA was first amplified for 3 additional

cycles using KAPA HiFi HotStart ReadyMix (KAPA Biosystems), 10 µM Partial Read1 primer and 10 µM non-poly dT primer (see **Supplementary Table 5** for primers). After SPRIselect clean-up, a locus-specific amplification (13 PCR cycles) was performed on the re-amplified cDNA using the generic forward SI-PCR primer (10 µM) and 10 µM of a locus-specific reverse primer for KRAS G12D/V mutation (**Supplementary Table 5**). The amplified locus-specific cDNAs are then cleaned using SPRI purification to remove unincorporated primers. Finally, the targeted amplicon libraries are generated through a PCR performed with a P5 generic forward PCR primer together with an RPI-x primer (10 µM each, **Supplementary Table 5**), as we previously described (45) The gene expression and targeted amplicon libraries were sequenced on a NovaSeq 6000 (Illumina, San Diego, CA). The cycle settings were as follows: 28 cycles for Read 1, 90 cycles for Read 2, 10 cycles for i7 sample index and 10 cycles for i5 sample index**.**

GoT gene expression data processing, alignment, clustering and cell-type assignment

The scRNA-seq libraries were processed with Cell Ranger (v7.0.1) using cellranger-count pipeline. The reads were aligned to the human genome GRCh38 with default parameters. The Seurat package(78) (v4.3.0) was used for downstream analysis using default parameters unless specified. Each sample dataset was analyzed separately. Briefly, cells with more than 20% mitochondrial genes and less than 100 detected genes were filtered out. Gene expression matrices were normalized, and top 2000 variable genes selected. Next, expression data was scaled and principal component analysis (PCA) was performed on the most variable genes. The resulting 30 principal components (PCs) were used for graph-based Louvain clustering to distinguish transcriptionally distinct cell groups. Cell types were manually assigned based on differentially expressed genes identified using the FindAllMarkers function using default settings (using top 2000 variable genes, in a minimum of 10% cells, using Wilcoxon rank sum test). They were annotated according to expression of known canonical lineage markers (e.g. **Fig. 1C**). Cell groups were visualized in a two-dimensional UMAP embedding. Doublets were predicted using the scDblFinder (79) v1.12.0) and DoubletFinder (80) (v2.0.3) R packages. Cells marked as doublets by both tools and showing mixed lineage marker expression were removed from downstream analysis.

IronThrone-GoT for processing targeted amplicon sequences and KRAS mutation calling

Analysis of the genotyping library was carried out as described previously (45) using IronThrone pipeline v2.1 (81). In brief, the primer sequence and the shared sequence (i.e., the expected sequence between the primer sequence and the mutation locus) are first searched for in the amplicon reads (Read 2). Then, the Read 1 sequences were scanned to look for any possible cell barcodes as per the cell barcode list from 10x Genomics. A mismatch of 20% was allowed for all sequence matching steps. Only UMIs with at least 2 or more supporting reads were retained for genotyping assignments, after the UMI collapse algorithm, as previously described (81,82). Filtered cells were finally assigned a genotype as follows: cells with at least one mutant UMI were

categorized as mutant cells whereas cells with no mutant UMI and at least one wildtype UMI were identified as wildtype.

Differential expression and gene set enrichment analysis

For statistical analysis, when the variable in question was genotype status (e.g., mutant versus wildtype), genotype status was entered as the fixed effect and samples as random effects in a linear mixed model. P-values were obtained from likelihood ratio tests of the full model with the effect in question against the model without the effect in question. Linear mixed effects analysis was performed using the lmerTest R package (83) (v.3.1-3). Differential gene expression testing between treated and untreated cells was performed using the logistic regression framework (84). For all analyses, the tested genes included the top 2,000 variable genes, which were filtered for those expressed in at least 10% of either group being tested. Volcano plot visualizations of differentially expressed genes were generated using the EnhancedVolcano (85) (v1.16.0) R package.

Pre-ranked gene set enrichment analysis (GSEA) was performed on gene ranking based on the sign of the fold change * -log10(P-value), using the fgsea (86) (v1.24.0) R package (hypergeometric test). Pathways considered correspond to the canonical Hallmark pathway genes from MSigDB database.

Gene module scoring

For examining gene module expression (e.g., inflammatory response, quiescence), the function AddModuleScore within the Seurat package was used to calculate the relative expression of genes of interest for each cell. To calculate the module expression of cell-cycle related genes, G2M phase and S phase marker genes were used as available in Seurat with CellCycleScoring function. Briefly, all analyzed genes were classified into bins based on average expression, and for each gene in the module, random genes from the same expression bin as the gene of interest were selected as control genes, as previously described (87). The expression of the control gene module was then subtracted from the average gene module expression of interest and considered as the module score.

Gene expression and module scores were visualized using violin plots or heatmaps (generated using the ComplexHeatmap (88) (v2.14.0) R package).

$CD83^+$ cell sorting and clonogenic assay culture

If fresh PBMCs were used, cells were isolated as per the mononuclear cell isolation protocol and then immediately prepared for staining. If frozen vials were used, multiple vials from the same patient (corresponding to different visits of the *KRAS*^{G12D} MDS patient) were thawed in a 37 °C water bath for 2 minutes. Vials were then reconstituted with 1mL of thawing media (25% FBS in

complete IMDM with 1% Penn Strep). Next, 15mL of thawing media was added dropwise to sample and cells were centrifuged for 5 minutes at 500 g. Cells were resuspended in 2mL of complete IMDM and then counted using AOPI (Revvity Health Sciences Inc. CS2-016-25ML). Cells were rested for two hours in the incubator (37 °C) at a concentration of 1 million cells/mL in a 6 well plate. After resting, cells were washed with media, collected, spun, and prepared for staining. Fully stained, unstained, and CD83 FMO was prepared to dictate gating strategy.
Cells were then stained with Trustain human Fc block (1:20, BioLegend 422301) for 15 minutes at room temperature. Without washing, antibodies were added to a final concentration of 1:100 (CD34, CD83, CD45, see **Supplementary Table 5** for antibody details). Cells with antibody cocktail were incubated at room temperature, in the dark, for 15 minutes. Cells were then washed in 1 mL of flow buffer, spun at 350g for 5 minutes, and then resuspended in 1 mL of flow buffer. CD83 positively and negatively sorted cells were collected in polypropylene tubes and left on ice until sorting was finished on the Thermo Bigfoot cell sorter. Freshly isolated sample totaled to 100,000 cells per sorting condition, while pooled samples totaled to 240,000 cells per sorting condition. Afterwards, cells from each sorted condition (and unsorted) were mixed into 3 mL MethoCult (Stemcell, H4435) and vortexed three times. Using a 3mL syringe with a 16 gauge blunt end needle (STEMCELL, 28810), the 3.3 mL mixture was distributed into 2 wells of a 6-well tissue culture plate. Photos of wells were taken on day 13 using the EVOS FL AUTO or EVOS M700. For colony counting, images were analyzed by hand according to established hematopoietic morphology criteria distinguishing between myelomonocytic and erythroid lineages. (Technical Manual, Human Colony-Forming Unit (CFU) Assays Using MethoCult™). Values of two duplicate wells were averaged.

Flow cytometry assessment of clonogenic assays

After 14 days of culture, 3 mL of flow buffer (4% FBS in PBS) was added to each well and incubated for 30 minutes at 37°C to dissolve the methocult. The following steps were done on ice: duplicate conditions were pooled and washed twice with 5 mL flow buffer for 15 minutes, 350g, 4 °C. A tenth of cells from each treated condition were collected for CD83 fluorescent minus one (FMO) control. Cells were then stained with Zombie NIR (1:4000 dilution; BioLegend, 423105) in PBS for 15 minutes at room temperature in the dark. Afterwards, cells were washed with 1 mL of flow buffer and then stained with an antibody cocktail (CD45, CD34, GlyA, CD14, CD71, CD11b, CD49d, and CD233, CD83 1:100 for each antibody, **see Supplementary Table 5**) for 15 minutes at room temperature, in the dark. All single-color controls were prepared from patient samples for each experiment and for every marker, except for CD83, CD233, and CD49d, for which single-color controls were prepared using UltraComp eBeads (eBioscience, 01-2222-42) stained with each antibody at a 1:100 dilution. Cells were washed with 1 mL of buffer, spun at 350g for 5 minutes, resuspended in 200 uL flow buffer, and filtered (Corning, CLS352235). All flow samples were acquired by Cytek Aurora or BD LSR II- Yellow. After sample acquisition, autofluorescence was extracted and samples were manually compensated using Spectroflo software. CD83 positive gates were dictated using CD83 FMO control. Note that erythrocytic populations were gated on $CD45^-$ to overcome red blood cell autofluorescence.

Genotyping mice

To genotype mice, ear clippings were digested in 100 uL of 25 mM NaOH at 95 °C for 1 hour. Solution was neutralized with equal volume of 40 mM Tris-HCl. Subsequently, a 15 uL PCR reaction was prepared: 2 uL of digested DNA, 5 uL of Gotaq Green Mastermix (M712C), 2 uM of tdTomato primers or KRAS G12D LSL primers (see **Supplementary Table 5**), and water. Touchdown PCR was run as follows: 94 °C 3 minutes; 10 cycles of 94 °C 30 seconds, 65 °C 30 seconds (-5 °C per cycle), 68 °C 45 seconds; 28 cycles of 94 °C 30 seconds, 60 °C 30 seconds, 72 °C 45 seconds; 72 °C 5 minutes; 12 °C hold. Concurrently, 2% agarose (Apex, 20-102GP) was prepared in 200 mL 1x TAE buffer by microwaving solution for 2 minutes. When the agarose mixture was clear, and temperature cooled down to 45 °C, 20 uL of 10 mg/mL SYBR Safe Gel Stain (Invitrogen, S33102) was added and prepared in a cast for gel electrophoresis. DNA ladder (New England biolabs Inc., N3231L) was mixed with loading dye (Gel Loading dye Purple 6X, no SDS, B7025S). DNA ladder and samples (10 uL) was loaded and the gel was run for 160 V for 30 minutes and imaged on gene sys software.

Harvesting and transducing cells for mouse line generation

This study was performed strictly following the recommendations in the Guide for the Care and Use of Laboratory Animals of the National Institutes of Health. All animals were handled according to approved institutional animal care and use committee (IACUC) protocols (00001517 and 00001560) of the Albert Einstein College of Medicine.

The protocol for transducing mouse bone marrow cells was adapted from a previously published work (89). A non-treated 12-well plate was coated with retronectin (r-fibronectin CH-296, Takara) diluted to 20 ug/mL in PBS (834 uL per well) and incubated overnight at 4 °C. Bone marrow cells were flushed from long bones of a Rosa26-LAL-tdTomato KRAS-LSLG12D mice using IMDM media (Fischer Scientific, 12440061) with 10% FBS, 1% Pen/Strep. Cells were spun down, mixed with 1 mL ACK lysing buffer (Gibco, A10492-01) for 5 minutes and then resuspended in 5 mL complete IMDM media. c-Kit$^+$ cells were isolated by adding 100 uL of CD117 Microbeads (Miltenyi, 130-097-146) for 30 minutes and following the manufacturer's protocol using LS column (130-042-401) placed on a MACS Multistand (130-042-303).

Pre-stimulation media was prepared StemSpan SFEM (STEMCELL, 09600), L-Glut (1%), Pen/Strep (2%), 50 ng/mL mSCF (Peprotech, 250-03), 50 ng/mL mTPO (Peprotech, 315-14), 50 ng/mL mFLT3 (Peprotech, 250-31L) and 25 ng/mL mIL3 (Peprotech, 213-13). A solution made of 10 ug polybrene (EMD Millipore, TR-1003-G) was added into 2 mL pre-stimulation media + 15 uL of virus (U of Iowa-5 Ad5CMVCre, titer $5x10^{10}$ PFU/mL, MOI of 110). Retronectin was removed from plate and the mixture of cells, pre-stimulation media, and virus, were equally distributed into 4 wells, spun at 900g, 37 °C, for 1 hour. After spinfection, cells were resuspended in media and incubated for 3 hours in 37 °C. Cells were then collected, spun at 5 minutes for 350g, and supernatant was discarded. 4 mL of warm pre-stimulation media was resuspended in the cell

pellet and cells were distributed into 4 wells for overnight incubation in the 12-well plate. Spinfection steps were repeated the next day. After 4 hours of resting, cells were collected, spun, counted, and resuspended in PBS to a final concentration of 1.75 million cells/mL

Transplantation of transduced cells

Using JL Shepherd I-68A research irradiator, C57BL6 6 mice were irradiated twice with 450 rads, 4 hours apart (females, 9 weeks old, n =4) (90). Recipient mice were transplanted intravenously with 100,000 - 350,000 cells in 200 uL PBS.

For secondary transplantation all long bone marrow cells of the primary engrafted donor mouse were flushed as previously described, lysed with ACK, counted, and diluted to 10 million cells/mL. These cells were transplanted intravenously into sub-lethally irradiated mice. Specifically, note that in **Fig. 6E**, 2 million cells in 200 uL PBS were intravenously transplanted into both male and female mice, secondary recipients (n=14). For **Fig. 6M**: 2 million cells in 200 uL PBS were transplanted into both female and male, 11 weeks old secondary recipients (n=11). Lastly, for **Fig. 8E,** note that 1 million cells in 200 uL PBS were transplanted into both female and male, secondary recipients (n=15).

Histological assessment of mouse terminal tissues

Long bones, left liver lobe, spleen, and tumors were fixed in 10% formalin for 1-3 days and then changed to 70% ethanol. Samples were then processed using standard hematoxylin (Poly Scientific R&D Corp. # S212-1GL) and eosin Y (Stat Lab, # SL98-1) staining, for protocol **see Supplementary Table 6.**

Mouse bone marrow aspiration

For femoral bone marrow aspirations, mice were anesthetized using Vet Equip anesthesia system (Vetequip V-10) and isoflurane. After the animals' leg was disinfected with 70% ethanol, a fine 27G needle (BD 305620) was inserted into the femoral bone marrow cavity through the distal condyles. A small volume (up to 10 uL) of bone marrow was gently aspirated using the 27G needle and kept in 50 uL PBS on ice. Animals received 5 mg/kg Meloxicam per subcutaneous injection as an analgesic.

Flow cytometry assessment of mouse tissues

Bone marrow aspirates of primary engrafted mice were spun down and the supernatant was removed. Remaining cells were lysed in 1 mL ACK on ice for 2 minutes. Cells were resuspended in 5 mL of flow buffer (4% FBS in PBS), then centrifuged at 350g at 4 °C. Cells were subsequently stained with Zombie NIR (1:4000 dilution; BioLegend, 423105) for 15 minutes in the dark. Cells were then washed with 1 mL of flow buffer, centrifuged at 350g for 5 minutes, and stained at a 1:100 dilution with an antibody cocktail prepared in a 1:1 mixture of Brilliant Stain Buffer (00-4409-42) and flow buffer (Sca-1, c-Kit, CD14, B220, CD83, Ter119, GR-1, CD150, CD11b, CD3, CD48, see **Supplementary Table 5** for antibody details). Cells were then washed with 1 mL, spun at 350g for 5 minutes, filtered, and acquired by the Cytek Aurora.

For termination of secondary engrafted mice all organs were harvested in PBS before processing. Mouse long bones were gently ground using mortar and pestle in 10 mL of PBS, washed with 5 mL of flow buffer, and filtered through a 70 uM (Fisherbrand, 22-363-548) filter. This process was repeated three times. Spleens and tumors were gently ground on a 70 um filter using a 5 mL syringe plunger (BD, 309646) and 15 mL of buffer. Peripheral blood, splenocytes, and BMCs were lysed using 1 mL of ACK (Gibco, A1049201) on ice for 3 minutes and then resuspended with 4% FBS in PBS (buffer). Each single cell suspension was spun at 350g, 4 °C for 5 minutes. Cells were stained with 1:4000 Zombie NIR (BioLegend, 423105) in PBS for 15 minutes in the dark in a 96-well plate. Cells were then washed with PBS, centrifuged at 350g, 4 °C, for 5 minutes, and stained with an antibody cocktail prepared in a 1:1 mixture of Brilliant Stain Buffer (00-4409-42) and flow buffer (Sca-1, CD16/CD32, c-kit, CD14, B220, CD83, Ter119, CD127, GR-1, CD34, CD150, CD11b, CD3, CD48). Cells were washed, spun, resuspended in 200 uL flow buffer and then acquired by the Cytek Aurora. Cells were passed through a filter (PALL Corporation, AcroPrep 8027).

Flow cytometric evaluation of frozen tissue

To evaluate the composition of the thymic tumor (**Fig. 6C**), frozen thymic cells (90% FBS, 10% DMSO) were removed from liquid nitrogen, thawed for 2 minutes, and 1mL of warm 25% FBS in RPMI was added to the tube dropwise. Contents were transferred to a larger tube and 10 mL of 10% FBS complete RPMI (1% P/S), spun at 350 g for 5 minutes, and then prepared for flow cytometry assessment described above.

CBC Analysis

Peripheral blood (35 uL) was collected, shaken three times, placed into a plasma tube (MiniCollect Tube, 0.25/0.5 mL K2EDTA) and then read by Oxford Science Genesis CBC Analyzer.

***In vivo* treatment with *KRAS* G12D-specific inhibitor**

For *in vivo* experiments, citric acid was prepared (pH=5) as per AAT Bioquest protocol (91) using sodium citrate dihydrate (Millipore Sigma, PHR1416-1G) and citric acid (Millipore Sigma, C1909). This solution was then titrated to pH of 5 with sodium hydroxide (ThermoFisher Scientific, 124260010). Two grams of SBE-β-CD (MedChemExpress, HY-17031) was added to 20 mL of citric acid (vehicle). To make 5 mg/mL stock of drug, 100 mg of MRTX1133 (MedChemExpress, HY-134813) was added to the vehicle solution by vortexing and then resting for 10 minutes. Vehicle and diluted MRTX1133 for *in vivo* experiments were stored in -20 °C for up to 5 months in amber tubes (USA Scientific, 1615-5507). The treatment was thawed, diluted threefold with vehicle to achieve a 10 mg/kg dose, and stored at 4 °C for no more than 3 days before use. Mice were treated with no more than 200 uL of drug or vehicle intraperitoneally (Becton Dickinson 329461).

***In vivo* treatment with CD83 neutralizing antibody**

For *in vivo* experiments, mice were treated with 300 ug/mouse of CD83 nAb (Bioxcell,BE0398)

or isotype control (Bioxcell, BE0088) twice a week, subcutaneously. Antibodies were stored in 4C and prepared immediately before injection using sterile saline. Mice were treated subcutaneously with no more than 200 uL of antibody (Becton Dickinson 329461).

Luminex

To prepare plasma, whole blood was collected into EDTA plasma collection tubes (MiniCollect Tube, 0.25/0.5 mL K2EDTA), gently inverted to mix, and centrifuged at 350 × g for 5 min. The plasma (supernatant) was carefully collected and stored at −20°C until further analysis. All samples were measured in technical duplicates and averaged for a final concentration. IFN-alpha, IFN-gamma, IL-1-beta, IL-6, IL-10, KC/GRO/CINC-1/CXCL1, MCP-1/CCL2 and TNF-alpha were measured using Millipore Sigma kit MCYT1-190K-08. Kits were used according to the manufacturer's instructions. Data were acquired on a Luminex Magpix XMAP Multiplex Reader (Luminex Technologies (Madison, WI, USA), RRID:SCR_023348) and were analyzed using Belysa Immunoassay Curve Fitting Software (Millipore Sigma, Burlington, MA, USA). Interpolated concentrations of all analytes were log-transformed before analysis to reduce non-normal skew and inter-assay variability. Samples were run at between 1-3x dilution and if the value was lower than the limit of detection, half the lowest standard was attributed as the value. Please see supplementary file 7 for raw data and where this addition was made. All cytokine data is shown in logarithmic scale.

ELISA

To assess the binding affinity of the antibodies targeting mouse and human CD83 to their respective ligands, recombinant Mouse CD83 (Kactus, CD8-MM283) or His-tagged Recombinant human CD83 (Sino biological 11763-H08H) were immobilized at a concentration of 1ug/mL in 1X coating buffer (Biolegend 421701) in a 96 well plate (96 well Microwell™ MaxiSorp™ flat bottom plate, Sigma Aldrich M5785) in the cold room overnight. After washing the plate 4X with washing buffer (TBS + 0.05% Tween20 + 2mM CaCl), the plate was blocked for one hour with blocking buffer (TBS +2mMCaCl + 1% BSA). After 4X washing, the plate was incubated with corresponding antibodies and respective isotype control (0.5 ug/mL of Celltheon, Syd Labs PA007125.05; 0.05 ug/mL Bioxcell BE0398, Bioxcell,BE0088) dissolved in TBS +2mMCaCl + 0.01% BSA) for one hour in blocking buffer at room temperate on a low speed orbital shaker. Plates were washed 4X with washing buffer and incubated with secondary antibody (mouse: 2500X dilution of goat-anti-Rat IgG HRP conjugate Cell Signaling 98164S or human: 10000X dilution of anti-human IgG HRP conjugate Sigma Aldrich A0170) for half an hour. After 5X washes (1 minute each) the plate was developed of TMB (Thermo Fisher, 34028) for five minutes before 2N of stop solution of H_2SO_4 was added. Plates were read at OD 450.

Statistics and reproducibility

Statistical details were indicated in the corresponding figure legends. P-values were adjusted with Benjamini-Hochberg (BH) FDR-correction unless specified otherwise. Statistical

significance was defined as a BH-adjusted p-value < 0.05 unless otherwise specified in the figure legends or methods section.

Data Availability

The processed sequencing data is available via Gene Expression Omnibus (GEO) under the accession number GSE299887. The accession token is **x**.

Acknowledgements: We thank the Einstein Flow Cytometry Core and especially Aodengtuya for her for her work on the sorter. We acknowledge the Cytek Aurora Analyzer from grant 1S10OD026833 and Thermo Bigfoot cell sorter grant 1S10OD032169. We also greatly thank Dave Reynolds from the Genomics Core for his work on preparing all samples for GoT. We thank the histology core for their contribution in this publication, which was supported by the Montefiore Einstein Cancer Center Support Grant of the National Institutes of Health under award number P30CA013330. Additionally, we are thankful for Rotem Alon, Vera DesMarais, and Hillary Guzik from the Analytical Imaging Facility (AIF) and acknowledge the use the 3DHistec Pannoramic 250 Flash III slide scanner: SIG #S10OD026852-01A1 and the Cancer Center grant: NCI cancer center support grant P30CA013330. We are grateful to Aakash Mahant Mahant, head of the Einstein CFAR biomarker core (funded by grant 5P30AI124414-05), for the luminex data. We thank Yiyu Zou for performing an *in vivo* toxicity test of both vehicle and drug. We are grateful to Hui for help with mouse irradiation. L.K. is supported by the Albert Einstein College of Medicine PhD Stipend Donor Fund. ASN is supported by Burroughs Wellcome Fund Career Award for Medical Scientists, National Institutes of Health Director's Early Independence Award, National Heart Lung and Blood Institute (R01 HL167139) and Starr Cancer Consortium. D.V. is supported by K12CA279871 NCI career developmental award and American Society of Hematology Scholar Award.

REFERENCES

1. Shastri A, Will B, Steidl U, Verma A. Stem and progenitor cell alterations in myelodysplastic syndromes. Blood. 2017;129:1586–94.
2. Elias HK, Schinke C, Bhattacharyya S, Will B, Verma A, Steidl U. Stem cell origin of myelodysplastic syndromes. Oncogene. 2014;33:5139–50.
3. Sereeaphinan C, Kanchanasuwan S, Julamanee J. Mortality-associated clinical risk factors in patients with febrile neutropenia: A retrospective study. IJID Regions. 2021;1:5–11.
4. Malcovati L, Della Porta MG, Strupp C, Ambaglio I, Kuendgen A, Nachtkamp K, et al. Impact of the degree of anemia on the outcome of patients with myelodysplastic syndrome and its integration into the WHO classification-based Prognostic Scoring System (WPSS). Haematologica. 2011;96:1433–40.
5. Platzbecker U, Kubasch AS, Homer-Bouthiette C, Prebet T. Current challenges and unmet medical needs in myelodysplastic syndromes. Leukemia. 2021;35:2182–98.

6. Desai P, Roboz GJ. Clonal Hematopoiesis and therapy related MDS/AML. Best Pract Res Clin Haematol. 2019;32:13–23.
7. Desai P, Mencia-Trinchant N, Savenkov O, Simon MS, Cheang G, Lee S, et al. Somatic mutations precede acute myeloid leukemia years before diagnosis. Nat Med. 2018;24:1015–23.
8. Genovese G, Kähler AK, Handsaker RE, Lindberg J, Rose SA, Bakhoum SF, et al. Clonal Hematopoiesis and Blood-Cancer Risk Inferred from Blood DNA Sequence. New England Journal of Medicine. 2014;371:2477–87.
9. Balandrán JC, Lasry A, Aifantis I. The Role of Inflammation in the Initiation and Progression of Myeloid Neoplasms. Blood Cancer Discov. 2023;4:254–66.
10. Nathan DI, Dougherty M, Bhatta M, Mascarenhas J, Marcellino BK. Clonal hematopoiesis and inflammation: A review of mechanisms and clinical implications. Crit Rev Oncol Hematol. 2023;192:104187.
11. Sango J, Carcamo S, Sirenko M, Maiti A, Mansour H, Ulukaya G, et al. RAS-mutant leukaemia stem cells drive clinical resistance to venetoclax. Nature. 2024;636:241–50.
12. Hamarsheh S, Osswald L, Saller BS, Unger S, De Feo D, Vinnakota JM, et al. Oncogenic KrasG12D causes myeloproliferation via NLRP3 inflammasome activation. Nat Commun. 2020;11:1659.
13. Jang G, Park R, Esteva E, Hsu P-F, Feng J, Upadhaya S, et al. Leukemogenic Kras mutation reprograms multipotent progenitors to facilitate its spread through the hematopoietic system. Journal of Experimental Medicine. 2025;222.
14. Karra L, Finger A-M, Shechtman L, Krush M, Meng-Yao Huang R, Prinz M, et al. Single-cell proteomics characterization of bone marrow hematopoiesis with distinct Ras pathway lesions. Blood Adv. 2025;9:4996–5008.
15. Chan IT, Kutok JL, Williams IR, Cohen S, Kelly L, Shigematsu H, et al. Conditional expression of oncogenic K-ras from its endogenous promoter induces a myeloproliferative disease. Journal of Clinical Investigation. 2004;113:528–38.
16. Braun BS, Tuveson DA, Kong N, Le DT, Kogan SC, Rozmus J, et al. Somatic activation of oncogenic *Kras* in hematopoietic cells initiates a rapidly fatal myeloproliferative disorder. Proceedings of the National Academy of Sciences. 2004;101:597–602.
17. Hochstetler CL, Feng Y, Sacma M, Davis AK, Rao M, Kuan C-Y, et al. KRasG12D expression in the bone marrow vascular niche affects hematopoiesis with inflammatory signals. Exp Hematol. 2019;79:3-15.e4.
18. Lasry A, Nadorp B, Fornerod M, Nicolet D, Wu H, Walker CJ, et al. An inflammatory state remodels the immune microenvironment and improves risk stratification in acute myeloid leukemia. Nat Cancer. 2022;
19. Sano H, Shimada A, Taki T, Murata C, Park M, Sotomatsu M, et al. RAS mutations are frequent in FAB type M4 and M5 of acute myeloid leukemia, and related to late relapse: a study of the Japanese Childhood AML Cooperative Study Group. Int J Hematol. 2012;95:509–15.
20. Prior IA, Hood FE, Hartley JL. The Frequency of Ras Mutations in Cancer. Cancer Res. 2020;80:2969–74.
21. Neubauer A, Dodge R, George S, Davey F, Silver R, Schiffer C, et al. Prognostic importance of mutations in the ras proto-oncogenes in de novo acute myeloid leukemia. Blood. 1994;83:1603–11.

22. Kadia TM, Kantarjian H, Kornblau S, Borthakur G, Faderl S, Freireich EJ, et al. Clinical and proteomic characterization of acute myeloid leukemia with mutated *RAS*. Cancer. 2012;118:5550–9.
23. Rivera D, Kim K, Kanagal-Shamanna R, Borthakur G, Montalban-Bravo G, Daver N, et al. Implications of <scp>RAS</scp> mutational status in subsets of patients with newly diagnosed acute myeloid leukemia across therapy subtypes. Am J Hematol. 2022;97:1599–606.
24. Alawieh D, Cysique-Foinlan L, Willekens C, Renneville A. RAS mutations in myeloid malignancies: revisiting old questions with novel insights and therapeutic perspectives. Blood Cancer J. 2024;14:72.
25. Padua R, Guinn B-A, Al-Sabah A, Smith M, Taylor C, Pettersson T, et al. RAS, FMS and p53 mutations and poor clinical outcome in myelodysplasias: a 10-year follow-up. Leukemia. 1998;12:887–92.
26. Dhillon V, Aguilar J, Kim P, Padmanabhan D, Yang J, Dyson G, et al. Clinical and Molecular Characteristics of RAS and RAS-like Mutational Signature in Acute Myeloid Leukemia. Blood. 2024;144:842–842.
27. Paschka P, Du J, Schlenk RF, Gaidzik VI, Bullinger L, Corbacioglu A, et al. Secondary genetic lesions in acute myeloid leukemia with inv(16) or t(16;16): a study of the German-Austrian AML Study Group (AMLSG). Blood. 2013;121:170–7.
28. Colgan JN, Peplinski JH, Kirkey DC, Lamble A, Ries RE, Meshinchi S. Contrasting Clinical Implications of NRAS Vs. KRAS Mutations in AML - Only KRAS Mutations Are Associated with Adverse Outcome. Blood. 2024;144:1555–1555.
29. Prior IA, Hood FE, Hartley JL. The Frequency of Ras Mutations in Cancer. Cancer Res. 2020;80:2969–74.
30. Jiang C, Wang H, Zhao J, Xu Y, Duan S. The role of RAS mutations in leukemia progression, differentiation, and drug resistance. Leuk Res Rep. 2026;25:100589.
31. Ward AF, Braun BS, Shannon KM. Targeting oncogenic Ras signaling in hematologic malignancies. Blood. 2012;120:3397–406.
32. McMahon CM, Ferng T, Canaani J, Wang ES, Morrissette JJD, Eastburn DJ, et al. Clonal Selection with RAS Pathway Activation Mediates Secondary Clinical Resistance to Selective FLT3 Inhibition in Acute Myeloid Leukemia. Cancer Discov. 2019;9:1050–63.
33. DiNardo CD, Tiong IS, Quaglieri A, MacRaild S, Loghavi S, Brown FC, et al. Molecular patterns of response and treatment failure after frontline venetoclax combinations in older patients with AML. Blood. 2020;135:791–803.
34. Amatangelo MD, Quek L, Shih A, Stein EM, Roshal M, David MD, et al. Enasidenib induces acute myeloid leukemia cell differentiation to promote clinical response. Blood. 2017;130:732–41.
35. Badar T, Patel KP, Thompson PA, DiNardo C, Takahashi K, Cabrero M, et al. Detectable FLT3-ITD or RAS mutation at the time of transformation from MDS to AML predicts for very poor outcomes. Leuk Res. 2015;39:1367–74.
36. Patnaik MM, Lasho T. Evidence-Based Minireview: Myelodysplastic syndrome/myeloproliferative neoplasm overlap syndromes: a focused review. Hematology. 2020;2020:460–4.
37. Mustafa Ali MK, Williams MT, Corley EM, AlKaabba F, Niyongere S. Impact of *KRAS* and *NRAS* mutations on outcomes in acute myeloid leukemia. Leuk Lymphoma. 2023;64:962–71.

38. Takahashi K, Jabbour E, Wang X, Luthra R, Bueso-Ramos C, Patel K, et al. Dynamic acquisition of FLT3 or RAS alterations drive a subset of patients with lower risk MDS to secondary AML. Leukemia. 2013;27:2081–3.
39. Zhou J-D, Yao D-M, Li X-X, Zhang T-J, Zhang W, Ma J-C, et al. *KRAS* overexpression independent of *RAS* mutations confers an adverse prognosis in cytogenetically normal acute myeloid leukemia. Oncotarget. 2017;8:66087–97.
40. Meggendorfer M, de Albuquerque A, Nadarajah N, Alpermann T, Kern W, Steuer K, et al. Karyotype evolution and acquisition of FLT3 or RAS pathway alterations drive progression of myelodysplastic syndrome to acute myeloid leukemia. Haematologica. 2015;100:e487–90.
41. Naranjo M, Mammadova J, Profitt S, Yelvington B, Brooks C, Kennedy K, et al. Impact of RAS mutations on outcomes in newly diagnosed AML patients. Blood. 2025;146:7026–7026.
42. Shen Q, Feng Y, Gong X, Jia Y, Gao Q, Jiao X, et al. A Phenogenetic Axis that Modulates Clinical Manifestation and Predicts Treatment Outcome in Primary Myeloid Neoplasms. Cancer Research Communications. 2022;2:258–76.
43. Ibrahim Elsayed SS, Deghady AA-M, Elneily DA, AboElwafa RAH. KRAS mutations in patients with AML: clinical characteristics and not reported mutations using NGS. Alexandria Journal of Medicine. 2024;60:186–91.
44. Warren JT, Link DC. Clonal hematopoiesis and risk for hematologic malignancy. Blood. 2020;
45. Nam AS, Kim K-T, Chaligne R, Izzo F, Ang C, Taylor J, et al. Somatic mutations and cell identity linked by Genotyping of Transcriptomes. Nature. 2019;571:355–60.
46. Breloer M, Fleischer B. CD83 regulates lymphocyte maturation, activation and homeostasis. Trends Immunol. 2008;29:186–94.
47. Li Z, Ju X, Silveira PA, Abadir E, Hsu W-H, Hart DNJ, et al. CD83: Activation Marker for Antigen Presenting Cells and Its Therapeutic Potential. Front Immunol. 2019;10.
48. Grosche L, Knippertz I, König C, Royzman D, Wild AB, Zinser E, et al. The CD83 Molecule – An Important Immune Checkpoint. Front Immunol. 2020;11.
49. Graham SM, Vass JK, Holyoake TL, Graham GJ. Transcriptional Analysis of Quiescent and Proliferating CD34+ Human Hemopoietic Cells from Normal and Chronic Myeloid Leukemia Sources. Stem Cells. Oxford University Press (OUP); 2007;25:3111–20.
50. Barreyro L, Will B, Bartholdy B, Zhou L, Todorova TI, Stanley RF, et al. Overexpression of IL-1 receptor accessory protein in stem and progenitor cells and outcome correlation in AML and MDS. Blood. American Society of Hematology; 2012;120:1290–8.
51. Uhlen M, Oksvold P, Fagerberg L, Lundberg E, Jonasson K, Forsberg M, et al. Towards a knowledge-based Human Protein Atlas. Nat Biotechnol. 2010;28:1248–50.
52. Shrestha B, Walton K, Reff J, Sagatys EM, Tu N, Boucher J, et al. Human CD83-targeted chimeric antigen receptor T cells prevent and treat graft-versus-host disease. Journal of Clinical Investigation. 2020;130:4652–62.
53. Betts B, Savid-Frontera C, McSain S, Walton K, Beatty N, Goala P, et al. CD83 CAR T overcome CD19 antigen loss in B cell malignancies after CD19-directed therapy. Blood. 2025;146:4098–4098.
54. Nagree MS, Zeng AGX, Varesi A, Lim INX, Shah S, Kim H, et al. Investigation of CD83 As a Novel Human Hematopoietic Stem Cell Inflammatory Activation Marker. Blood. 2023;142:4067–4067.

55. Abplanalp WT, Cremer S, John D, Hoffmann J, Schuhmacher B, Merten M, et al. Clonal Hematopoiesis-Driver DNMT3A Mutations Alter Immune Cells in Heart Failure. Circ Res. Lippincott Williams and Wilkins; 2021;128:216–28.
56. Wang Y, Meng Y, Chen K, Li A, Yan J, Ding J, et al. Pan-cancer single-cell transcriptomic analysis reveals CD83 as a hallmark of tumor-associated neutrophils with senescent and pro-tumor properties. Comput Struct Biotechnol J. 2025;27:4615–32.
57. Vizeacoumar FJ, Arnold R, Vizeacoumar FS, Chandrashekhar M, Buzina A, Young JTF, et al. A negative genetic interaction map in isogenic cancer cell lines reveals cancer cell vulnerabilities. Mol Syst Biol. 2013;9:696.
58. Ling J, Kang Y, Zhao R, Xia Q, Lee D-F, Chang Z, et al. KrasG12D-Induced IKK2/β/NF-κB Activation by IL-1α and p62 Feedforward Loops Is Required for Development of Pancreatic Ductal Adenocarcinoma. Cancer Cell. 2012;21:105–20.
59. Barbie DA, Tamayo P, Boehm JS, Kim SY, Moody SE, Dunn IF, et al. Systematic RNA interference reveals that oncogenic KRAS-driven cancers require TBK1. Nature. 2009;462:108–12.
60. Li Z, Abadir E, Lee K, Clarke C, Bryant CE, Cooper W, et al. Targeting CD83 in mantle cell lymphoma with anti-human CD83 antibody. Clin Transl Immunology. 2020;9.
61. Dudziak D, Kieser A, Dirmeier U, Nimmerjahn F, Berchtold S, Steinkasserer A, et al. Latent membrane protein 1 of Epstein-Barr virus induces CD83 by the NF-kappaB signaling pathway. J Virol. 2003;77:8290–8.
62. von Wulffen M, Luehrmann V, Robeck S, Russo A, Fischer-Riepe L, van den Bosch M, et al. S100A8/A9-alarmin promotes local myeloid-derived suppressor cell activation restricting severe autoimmune arthritis. Cell Rep. 2023;42:113006.
63. Chakraborty S, Shapiro LC, de Oliveira S, Rivera-Pena B, Verma A, Shastri A. Therapeutic targeting of the inflammasome in myeloid malignancies. Blood Cancer J. 2021;11:152.
64. Hurtado-Navarro L, Cuenca-Zamora EJ, Zamora L, Bellosillo B, Such E, Soler-Espejo E, et al. NLRP3 inflammasome activation and symptom burden in KRAS-mutated CMML patients is reverted by IL-1 blocking therapy. Cell Rep Med. 2023;4:101329.
65. Ohanian M, Faderl S, Ravandi F, Pemmaraju N, Garcia-Manero G, Cortes J, et al. Is acute myeloid leukemia a liquid tumor? Int J Cancer. 2013;133:534–43.
66. Loscocco GG, Vannucchi AM. Myeloid sarcoma: more and less than a distinct a. Ann Hematol. 2023;102:1973–84.
67. Kindler T, Cornejo MG, Scholl C, Liu J, Leeman DS, Haydu JE, et al. K-RasG12D–induced T-cell lymphoblastic lymphoma/leukemias harbor Notch1 mutations and are sensitive to γ-secretase inhibitors. Blood. 2008;112:3373–82.
68. Sabnis AJ, Cheung LS, Dail M, Kang HC, Santaguida M, Hermiston ML, et al. Oncogenic Kras Initiates Leukemia in Hematopoietic Stem Cells. PLoS Biol. 2009;7:e1000059.
69. Zhang J, Wang J, Liu Y, Sidik H, Young KH, Lodish HF, et al. Oncogenic Kras-induced leukemogeneis: hematopoietic stem cells as the initial target and lineage-specific progenitors as the potential targets for final leukemic transformation. Blood. 2009;113:1304–14.
70. Dail M, Li Q, McDaniel A, Wong J, Akagi K, Huang B, et al. Mutant *Ikzf1, Kras* ^{G12D} , and *Notch1* cooperate in T lineage leukemogenesis and modulate responses to targeted agents. Proceedings of the National Academy of Sciences. 2010;107:5106–11.

71. Van Meter MEM, Díaz-Flores E, Archard JA, Passegué E, Irish JM, Kotecha N, et al. K-RasG12D expression induces hyperproliferation and aberrant signaling in primary hematopoietic stem/progenitor cells. Blood. 2007;109:3945–52.
72. Akutagawa J, Huang TQ, Epstein I, Chang T, Quirindongo-Crespo M, Cottonham CL, et al. Targeting the PI3K/Akt pathway in murine MDS/MPN driven by hyperactive Ras. Leukemia. 2016;30:1335–43.
73. Lyubynska N, Gorman MF, Lauchle JO, Hong WX, Akutagawa JK, Shannon K, et al. A MEK Inhibitor Abrogates Myeloproliferative Disease in *Kras* Mutant Mice. Sci Transl Med. 2011;3.
74. Braun BS, Archard JA, Van Ziffle JAG, Tuveson DA, Jacks TE, Shannon K. Somatic activation of a conditional KrasG12D allele causes ineffective erythropoiesis in vivo. Blood. 2006;108:2041–4.
75. Nann D, Schade T, Overkamp M, Mahmutovic L, Bag E, Forchhammer S, et al. Myeloid sarcoma shows a high frequency of mutations activating the <scp>MAPK</scp> / <scp>ERK</scp> pathway and association with clonal hematopoiesis. J Pathol Clin Res. 2025;11.
76. Lasry A, Nadorp B, Loghavi S, Patel R, Mansour H, Kelly B, et al. Exploiting RAS pathway addiction as a therapeutic vulnerability in myeloid sarcoma. Blood. 2025;146:220–220.
77. Nadorp B, Lasry A, Loghavi S, Patel R, Mansour H, Rovatti PE, et al. RAS pathway activation and microenvironmental adaptation as hallmarks of myeloid sarcoma. Blood Cancer Discov. 2026;
78. Hao Y, Hao S, Andersen-Nissen E, Mauck WM, Zheng S, Butler A, et al. Integrated analysis of multimodal single-cell data. Cell. 2021;184:3573-3587.e29.
79. Germain P-L, Lun A, Garcia Meixide C, Macnair W, Robinson MD. Doublet identification in single-cell sequencing data using scDblFinder. F1000Res. 2022;10:979.
80. McGinnis CS, Murrow LM, Gartner ZJ. DoubletFinder: Doublet Detection in Single-Cell RNA Sequencing Data Using Artificial Nearest Neighbors. Cell Syst. 2019;8:329-337.e4.
81. Nam AS, Dusaj N, Izzo F, Murali R, Myers RM, Mouhieddine TH, et al. Single-cell multi-omics of human clonal hematopoiesis reveals that DNMT3A R882 mutations perturb early progenitor states through selective hypomethylation. Nat Genet. 2022;54:1514–26.
82. Smith T, Heger A, Sudbery I. UMI-tools: modeling sequencing errors in Unique Molecular Identifiers to improve quantification accuracy. Genome Res. 2017;27:491–9.
83. Kuznetsova A, Brockhoff PB, Christensen RHB. lmerTest Package: Tests in Linear Mixed Effects Models. J Stat Softw. 2017;82.
84. Ntranos V, Yi L, Melsted P, Pachter L. A discriminative learning approach to differential expression analysis for single-cell RNA-seq. Nat Methods. 2019;16:163–6.
85. Blighe K RSLM. EnhancedVolcano: Publication-ready volcano plots with enhanced colouring and labeling. R package version 1.24.0. https://github.com/kevinblighe/EnhancedVolcano. 2024;
86. Korotkevich G, Sukhov V, Budin N, Shpak B, Artyomov MN, Sergushichev A. Fast gene set enrichment analysis. 2016.
87. Tirosh I, Izar B, Prakadan SM, Wadsworth MH, Treacy D, Trombetta JJ, et al. Dissecting the multicellular ecosystem of metastatic melanoma by single-cell RNA-seq. Science (1979). 2016;352:189–96.

88. Gu Z, Eils R, Schlesner M. Complex heatmaps reveal patterns and correlations in multidimensional genomic data. Bioinformatics. 2016;32:2847–9.
89. Mitchell K, Barreyro L, Todorova TI, Taylor SJ, Antony-Debré I, Narayanagari S-R, et al. IL1RAP potentiates multiple oncogenic signaling pathways in AML. Journal of Experimental Medicine. 2018;215:1709–27.
90. Brodin NP, Chen Y, Yaparpalvi R, Guha C, Tomé WA. Dosimetry Formalism and Implementation of a Homogenous Irradiation Protocol to Improve the Accuracy of Small Animal Whole-Body Irradiation Using a 137Cs Irradiator. Health Phys. 2016;110:S26–38.
91. AAT Bioquest Inc,. Quest Calculate™ Citrate Buffer (pH 3.0 to 6.2) Preparation and Recipe. 2025.

Figure 1

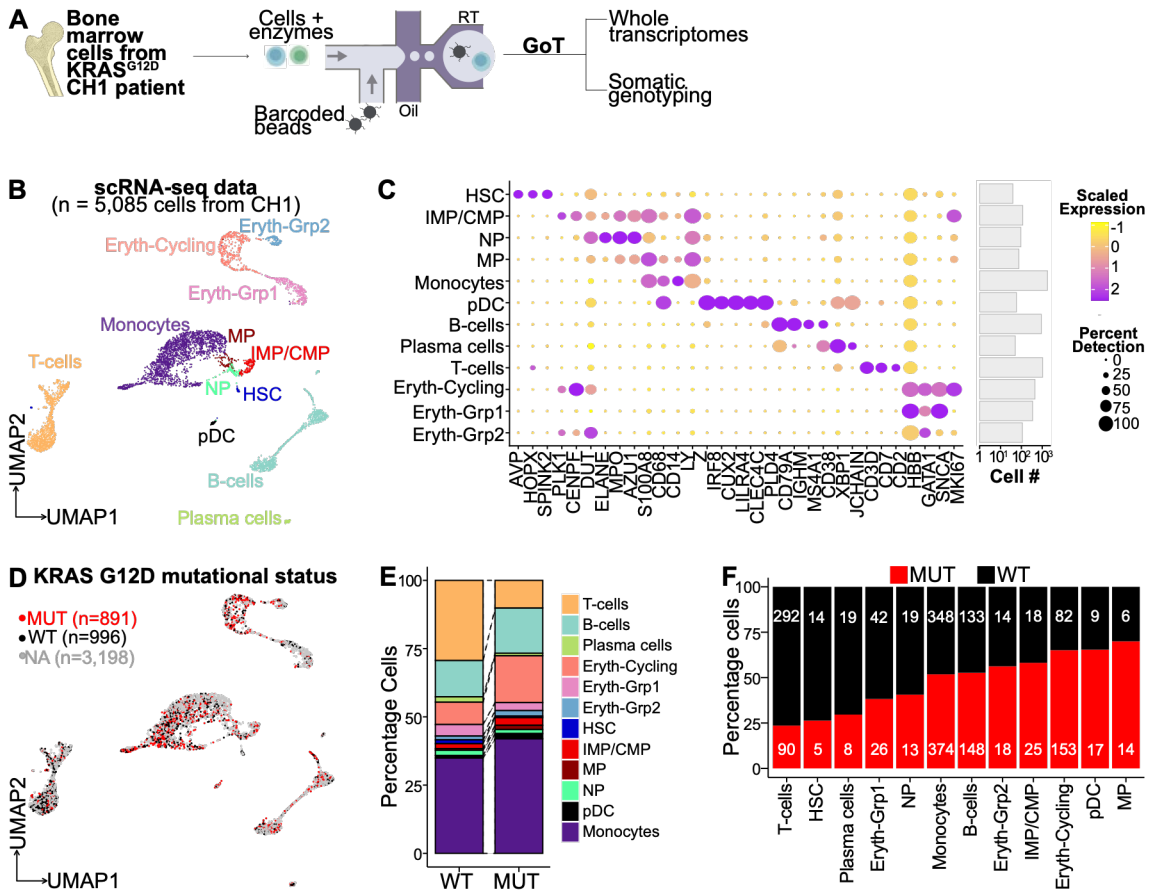


Figure 1. *KRAS*^{G12D} mutated cells in clonal hematopoiesis are overrepresented in the monocytic compartment.

A. Schematic of experimental design for profiling bone marrow cells from *KRAS*^{G12D}-mutant clonal hematopoeisis (CH) patient.

B. Uniform Manifold Approximation and Projection (UMAP) of bone marrow cells from CH1 patient (n = 5,085 cells), overlaid with cell type assignment. HSC, Hematopoeitic Stem Cells; CMP, common myeloid progenitors; Eryth, erythrocytes; IMP, immature myeloid progenitors; Mono, Monocytes; MP, myeloid progenitors; NP, neutrophilic progenitors; pDC, plasmacytoid dendritic cells.

C. Dot plot showing expression levels of cell type specific gene markers in each cell group (right panel). Bar plot showing number of cells per cell group (left panel).

D. UMAP of bone marrow cells from primary CH sample overlaid with *KRAS* mutational status. MUT: mutant; WT: wild-type; NA: unprofiled.

E. Bar plot showing percentage of cells from each cell type among *KRAS* G12D-mutant (MUT) and wildtype (WT) cells.
F. Bar plot showing the distribution of KRAS G12D-mutant (MUT) and wildtype (WT) cells in each cell type. Numbers within bars correspond to number of MUT or WT cells. HSC, Hematopoietic Stem Cells; Eryth, erythrocytes; CMP, common myeloid progenitors; IMP, immature myeloid progenitors; MP, myeloid progenitors; NP, neutrophilic progenitors; pDC, plasmacytoid dendritic cells.

Figure 2

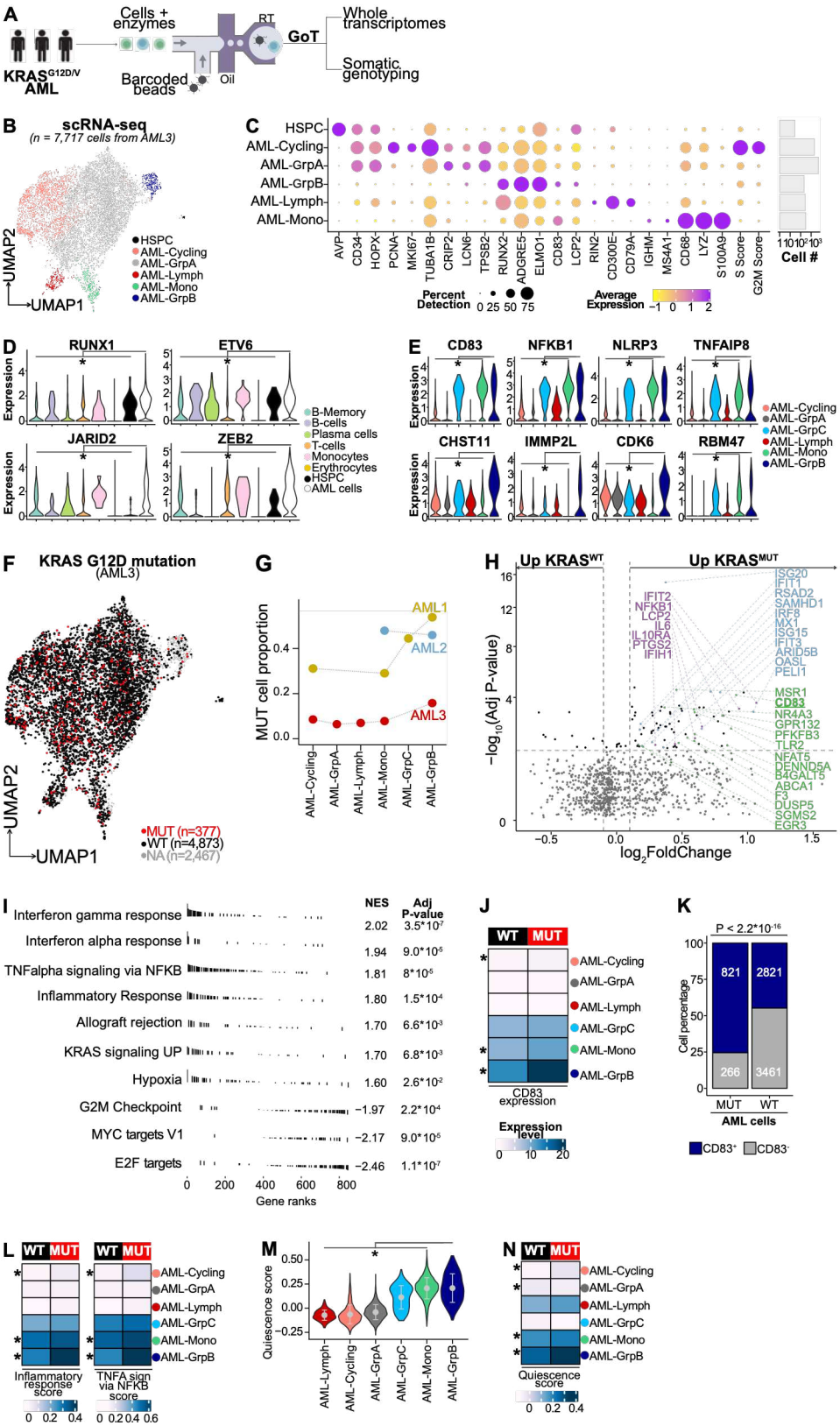

A
Cells + enzymes
RT
GoT
Whole transcriptomes
Somatic genotyping
KRAS G12D/V AML
Barcoded beads
Oil
B
scRNA-seq
(n = 7,717 cells from AML3)
UMAP2
UMAP1
HSPC
AML-Cycling
AML-GrpA
AML-Lymph
AML-Mono
AML-GrpB
C
HSPC
AML-Cycling
AML-GrpA
AML-GrpB
AML-Lymph
AML-Mono
AVP CD34 HOPX PCNA MKI67 TUBA1B CRIP2 LCN6 TPSB2 RUNX2 ADGRE5 ELMO1 CD83 LCP2 RIN2 CD300E CD79A IGHM MS4A1 CD68 LYZ S100A9 S Score G2M Score
Cell #
Percent Detection 0 25 50 75
Average Expression −1 0 1 2
D
RUNX1
ETV6
JARID2
ZEB2
Expression
B-Memory
B-cells
Plasma cells
T-cells
Monocytes
Erythrocytes
HSPC
AML cells
E
CD83
NFKB1
NLRP3
TNFAIP8
CHST11
IMMP2L
CDK6
RBM47
Expression
AML-Cycling
AML-GrpA
AML-GrpC
AML-Lymph
AML-Mono
AML-GrpB
F
KRAS G12D mutation
(AML3)
UMAP2
UMAP1
MUT (n=377)
WT (n=4,873)
NA (n=2,467)
G
MUT cell proportion
AML1
AML2
AML3
AML-Cycling AML-GrpA AML-Lymph AML-Mono AML-GrpC AML-GrpB
H
Up KRAS^WT
Up KRAS^MUT
−log10(Adj P-value)
log2FoldChange
IFIT2 NFKB1 LCP2 IL6 IL10RA PTGS2 IFIH1
ISG20 IFI1 RSAD2 SAMHD1 IRF8 MX1 ISG15 IFIT3 ARID5B OASL PELI1
MSR1 CD83 NR4A3 GPR132 PFKFB3 TLR2 NFAT5 DENND5A B4GALT5 ABCA1 F3 DUSP5 SGMS2 EGR3
I
NES
Adj P-value
Interferon gamma response 2.02 3.5*10-7
Interferon alpha response 1.94 9.0*10-5
TNFalpha signaling via NFKB 1.81 8*10-5
Inflammatory Response 1.80 1.5*10-4
Allograft rejection 1.70 6.6*10-3
KRAS signaling UP 1.70 6.8*10-3
Hypoxia 1.60 2.6*10-2
G2M Checkpoint −1.97 2.2*10-4
MYC targets V1 −2.17 9.0*10-5
E2F targets −2.46 1.1*10-7
Gene ranks
J
WT MUT
AML-Cycling
AML-GrpA
AML-Lymph
AML-GrpC
AML-Mono
AML-GrpB
CD83 expression
Expression level
K
P < 2.2*10-16
Cell percentage
821 2821 266 3461
MUT WT
AML cells
CD83+ CD83-
L
WT MUT
Inflammatory response score
TNFA sign via NFKB score
M
Quiescence score
AML-Lymph AML-Cycling AML-GrpA AML-GrpC AML-Mono AML-GrpB
N
WT MUT
Quiescence score

Figure 2. **Inflammatory *KRAS*^{G12D} mutated cells in AML are characterized by CD83 overexpression.**

A. Schematic of experimental design for profiling cells from three *KRAS* G12D/V-mutant AML patients (AML 1-3).

B. Uniform Manifold Approximation and Projection (UMAP) of cells from one representative AML sample (AML3, n = 7,717 cells), overlaid with cell type assignment. HSPC, Hematopoeitic stem and progenitor cells; AML-Lymph, AML cells with lymphoid differentiation; AML-Mono, AML cells with myeloid differentiation.

C. Dot plot showing expression levels of cell type specific gene markers in each cell group from AML3 sample (left panel). Bar plot showing number of cells per cell group (right panel).

D. Violin plot showing expression of leukemic markers per cell type across all samples. P-value from Wilcoxon rank sum test comparing expression in AML cells to all other cells, *: p-value < 0.05.

E. Violin plot showing expression of markers of AML-GrpB cells per AML cell state from all samples. P-value from Wilcoxon rank sum test comparing expression in AML-GrpB cells to all other AML cells, *: p-value < 0.05.

F. UMAP of cells from AML3 sample overlaid with *KRAS* mutational status (left panel). Bar plot showing proportion mutant or wildtype cells across each cell type (right panel). Cell numbers are highlighted within each bar in white. MUT: mutant; WT: wild-type; NA: unprofiled.

G. High proportion of *KRAS* G12D/V-mutant cells among AML-GrpB cells. Proportion calculated as ratio of mutant cell number in an AML cell state to total cell number in that state.

H. Volcano plot showing genes differentially expressed (DE) between *KRAS* G12D/V-mutant and wildtype AML cells via linear mixed model (LMM) with/without mutation status (**methods**). Highlighted in green are inflammation genes, in blue interferon response genes and in purple genes involved in both. Adjusted p-values correspond to p-values corrected for multiple testing via Benjamini-Hochberg adjustment.

I. Enrichment of inflammation and interferon pathways highlighted by pre-ranked gene set enrichment analysis using the MSigDB Hallmark collection (hypergeometric test, **methods**). Genes DE between *KRAS* G12D-mutant and wildtype AML cells analyzed as in **Fig. 2H**. NES corresponds to the normalized enrichment score from the pre-ranked GSEA. Adjusted p-values correspond to p-values corrected for multiple testing via Benjamini-Hochberg adjustment.

J. Heatmap showing *CD83* expression in *KRAS* G12D/V-mutant AML cells. P-value from Wilcoxon rank sum test, *: p-value < 0.05.

K. Bar plot showing proportion of CD83-expressing cells among *KRAS* G12D/V mutant or wildtype AML cells. Cell numbers are highlighted within each bar in white. P-value from Fisher exact test.

L. Heatmap showing module scores related to inflammation in *KRAS* G12D/V-mutant AML cell states. Inflammatory genes (Inflammatory response and TNFA signaling via NFKB) from MSigDB Hallmark pathways. P-value from Wilcoxon rank sum test, *: p-value < 0.05.

M. Violin plot showing quiescence module score in AML cell states from all samples. P-value from Wilcoxon rank sum test comparing score in AML-GrpB to other AML cells, *: p-value < 0.05. Signature genes correspond to genes upregulated in quiescent versus dividing CD34+ cells isolated from peripheral blood of normal donors (49).
N. Heatmap showing quiescence module score in *KRAS* G12D/V-mutant AML cells. P-value from Wilcoxon rank sum test, *: p-value < 0.05. Signature genes as in **Fig. 2L**.

Figure 3

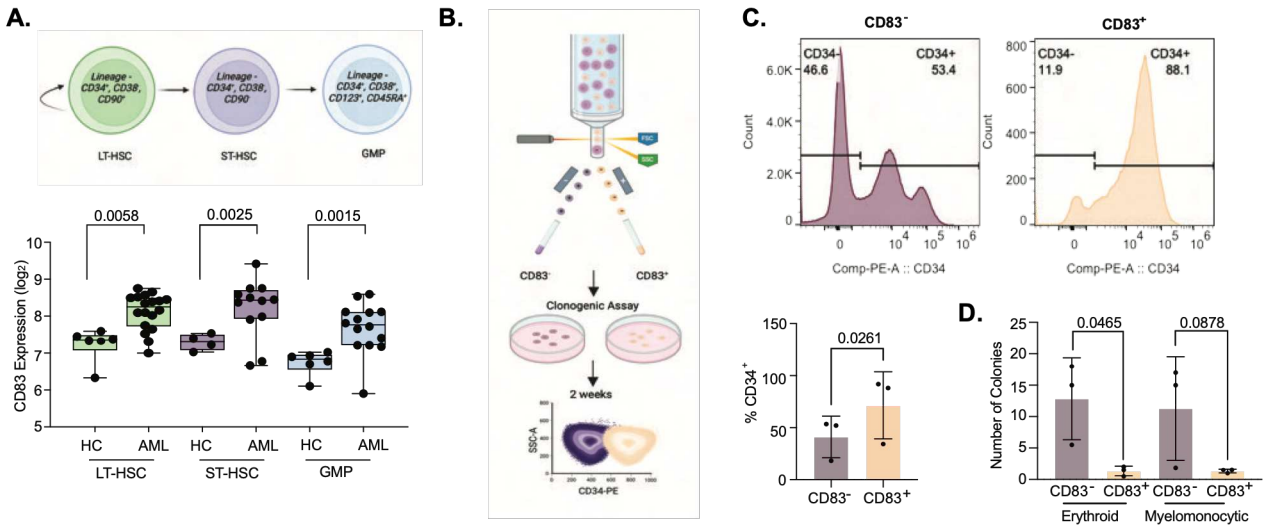


Figure 3: CD83^{+} sorted cells have increased CD34 expression but decreased colony counts.
A. Schematic illustrating sorting strategy for stem and progenitor cells from healthy controls (HC, n=4-6) and AML patients (top panel, n=12-18). Scheme generated in biorender.com. Box plots showing CD83 expression in each of the sorted cell populations (bottom panel). P-values from Wilcoxon rank sum test. LT-HSC, Long-Term Hematopoeitic Stem Cells (HSC); ST-HSC, Short-Term HSC; GMP, Granulocyte-monocyte progenitors. Healthy
B. Schematic illustrating sorting strategy and experimental design for cells from MDS *KRAS*^{G12D} PBMCs. Scheme generated in biorender.com.
C. Representative flow cytometry histogram demonstrating CD34 expression in live cells in each sorted cell condition (top panels, **C1**). Bar plots showing percentage of CD34-expressing cells (CD34+) (Bottom panel, **C2**). n = 3 biological replicates. P-value from paired one-tail t-test.
D. Bar plot showing erythroid and myeloid colony counts in each sorted condition. Clonogenic assay, n = 3 biological replicates. Representative images in **Supplementary Fig. 4D**. P-values from paired one-tail t-test.

Figure 4

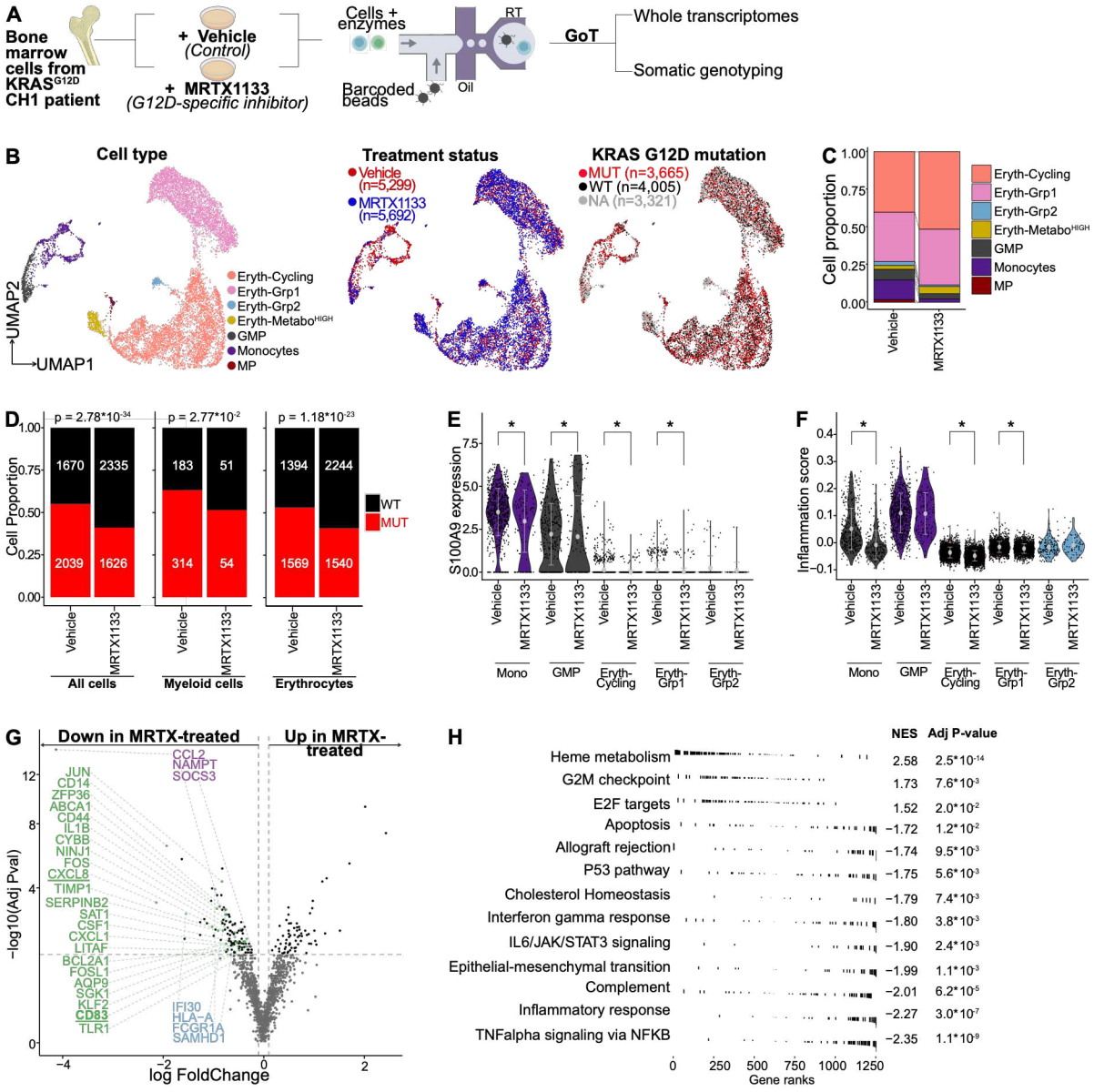


Figure 4. *KRAS*^{G12D} inhibition reverses inflammation and relieves the erythroid differentiation block in patient samples on the single cell level.

A. Schematic of experimental design for profiling *KRAS*^{G12D}-mutant cells from CH1 patient treated or not with 100 nM MRTX1133, a *KRAS*-G12D specific inhibitor.

B. Uniform Manifold Approximation and Projection (UMAP) of cells from CH1 patient treated or not with MRTX1133 (n = 10,991 cells), overlaid with cell type assignment (left panel), treatment status (middle panel) and *KRAS* mutational status (right panel). Eryth: Erythrocytes, GMP: Granulocyte-Monocyte Progenitors, MP: Myeloid Progenitors.

C. Bar plot showing differences in cell type proportion upon MRTX1133 treatment.

D. Bar plot showing decreased proportion of *KRAS*^{G12D} mutant cells upon KRAS inhibition, across all cells (left panel), myeloid cells (middle panel) and erythrocytes (right panel). P-values from Fisher exact test.
E. Violin plot showing expression of *S100A9* in each cell type upon MRTX1133 treatment. P-value from Wilcoxon rank sum test, *: p-value < 0.05.
F. Violin plot showing inflammatory module score upon MRTX1133 treatment. Inflammatory genes from Inflammatory Response pathway from MSigDB Hallmark database. P-value from Wilcoxon rank sum test, *: p-value < 0.05.
G. Volcano plot showing genes differentially expressed (DE) between MRTX1133-treated and untreated *KRAS*-mutant GMPs via Logistic Regression model (**methods**). Highlighted in green are inflammation genes, in blue interferon response genes and in purple genes involved in both. Adjusted p-values correspond to p-values corrected for multiple testing via Benjamini-Hochberg adjustment.
H. Downregulation of inflammation and interferon pathways in *KRAS*-mutant GMPs treated with MRTX1133, highlighted by pre-ranked gene set enrichment analysis (GSEA) using the MSigDB Hallmark collection (hypergeometric test, **methods**). DE genes from **Fig. 4G** analyzed. NES corresponds to the normalized enrichment score from the pre-ranked GSEA. Adjusted p-values correspond to p-values corrected for multiple testing via Benjamini-Hochberg adjustment.

Figure 5

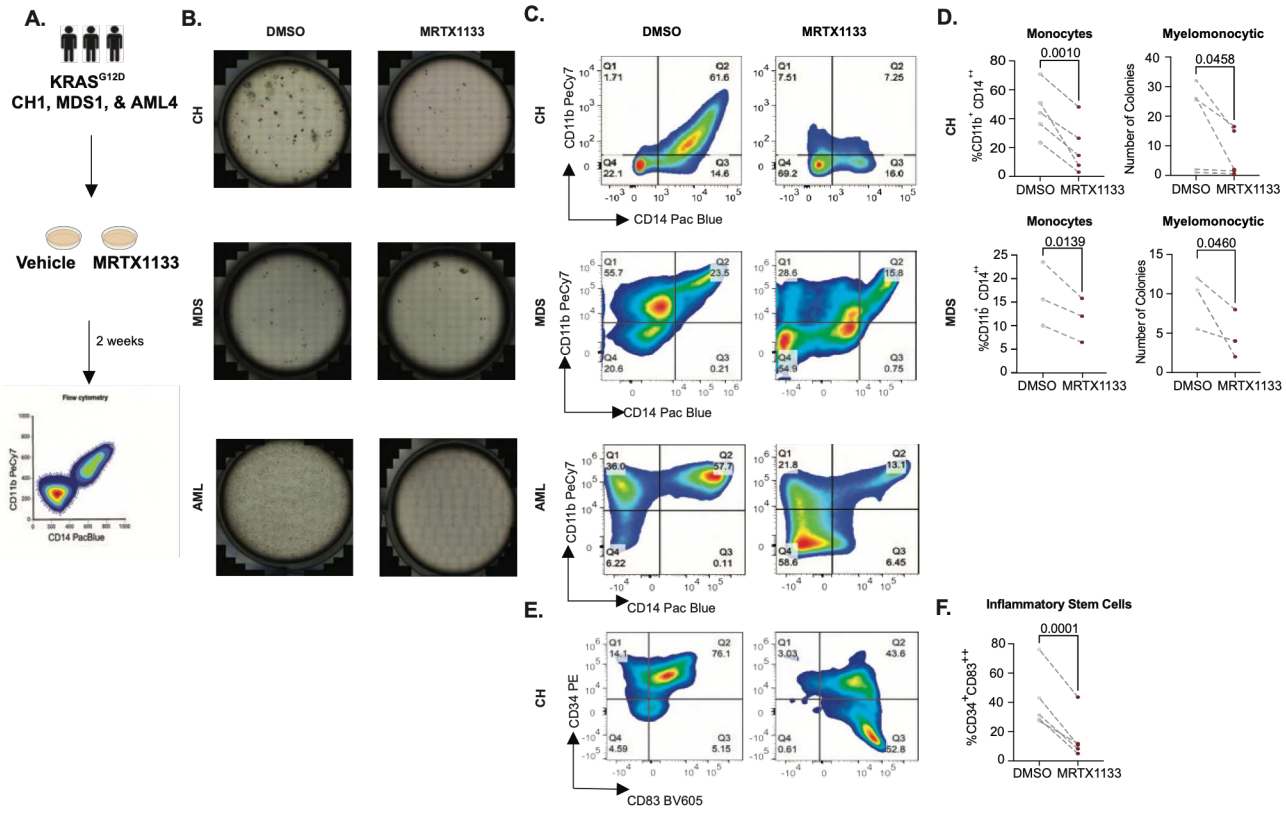


Figure 5: *KRAS*^{G12D} inhibition reverses decreased myeloid cells in different subtypes of KRAS^{G12D} hematological disorders *in vitro*.

A. Experimental design of KRAS G12D mutant CH and AML patient samples treated or not with MRTX1133 *in vitro*. Schematic created in Biorender.com

B. Representative images of patient samples treated with DMSO or 500 nM MRTX1133 taken with EVOS M700 and EVOS FL AUTO. CH1: BMCs from Clonal Hematopoesis patient (same patient as in Fig. 1 and Fig. 4). AML4: CD3-CD19- PBMCs from an AML patient with Mixed Myeloid Leukemia (MLL)/KMT23A (see Supplementary Table 1 for sample details).

C. Representative flow cytometry analysis of myeloid markers in CD3-CD19- PBMCs (AML4), BMCs/PBMCs (CH1), and PBMCs (MDS1) treated with DMSO or 500 nM MRTX1133. Myeloid cells are gated on CD45+ using CD11b and CD14 markers. See Supplementary Fig. 6A for other MRTX1133 concentrations.

D. Cumulative colony assay flow data on MDS cells (n=3 biological replicates, left panel) and CH1 cells treated with DMSO or 500 nM MRTX1133 (n=5 biological replicates, left panel). Number of myelomonocytic colonies among MDS (n=3 biological replicates, right panel) and

CH1 patient treated cells (n=5 biological replicates, right panel) with DMSO and 500 nM MRTX1133. P-value from linear mixed model (LMM).

E. Representative flow cytometry analysis of inflammatory stem cells in CH1 BMCs/PBMCs treated with DMSO or 500 nM MRTX1133. Cells are gated on CD45+ using CD34 and CD83 markers.

F. Cumulative colony assay flow data on CH1 cells treated with DMSO or 500 nM MRTX1133 (n=3 biological replicates). P-value from linear mixed model (LMM).

Figure 6

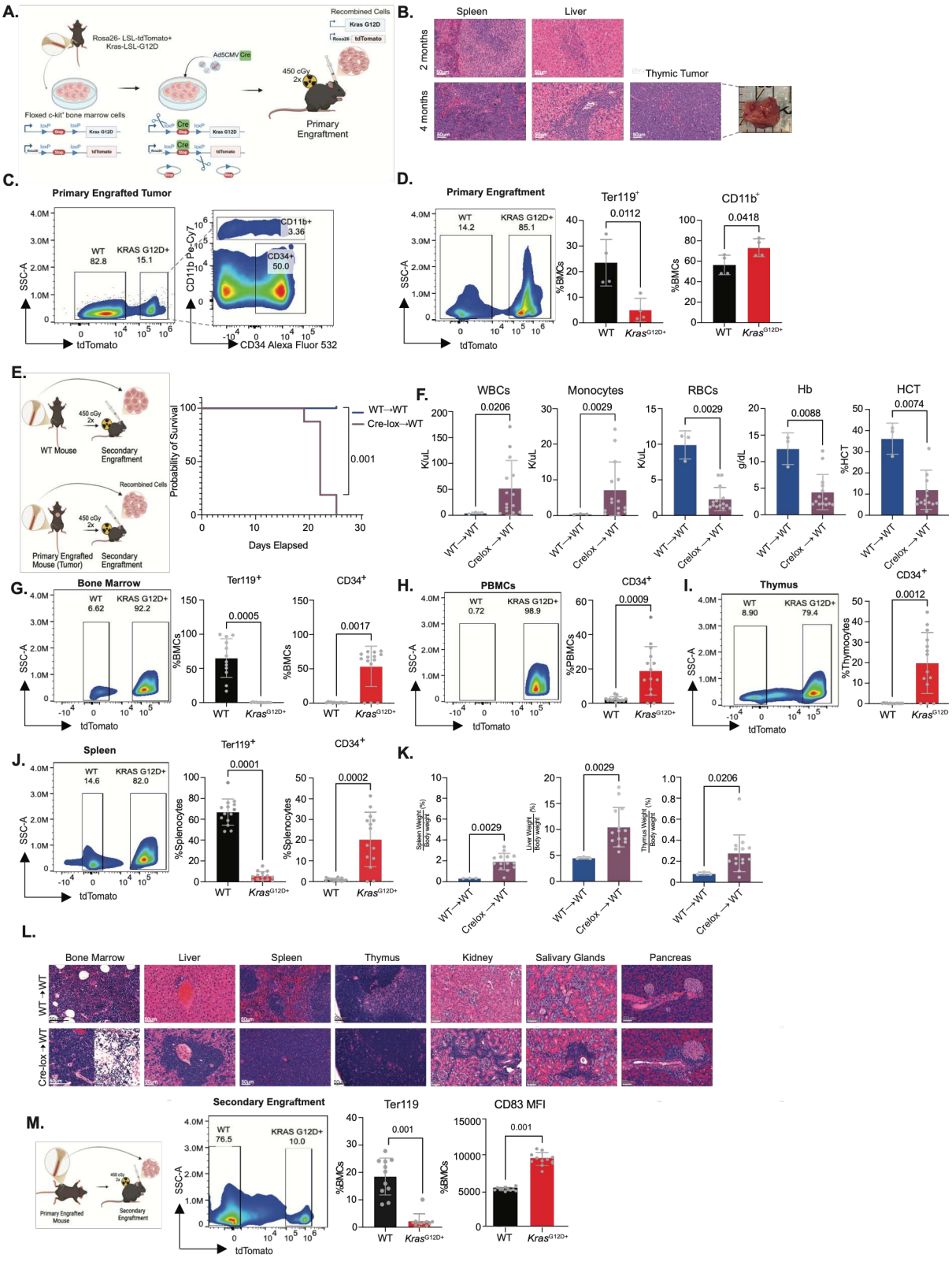

A.
Recombined Cells
Kras G12D
tdTomato
Rosa26- LSL-tdTomato+
Kras-LSL-G12D
Ad5CMV Cre
Floxed c-kit+ bone marrow cells
450 cGy
2x
Primary
Engraftment
B.
Spleen
Liver
2 months
4 months
Thymic Tumor
C.
Primary Engrafted Tumor
WT
82.8
KRAS G12D+
15.1
SSC-A
tdTomato
CD11b+
3.36
CD34+
50.0
CD11b Pe-Cy7
CD34 Alexa Fluor 532
D.
Primary Engraftment
WT
14.2
KRAS G12D+
85.1
%BMCs
Ter119+
0.0112
CD11b+
0.0418
WT
KrasG12D+
E.
WT Mouse
Secondary
Engraftment
Recombined Cells
Primary Engrafted
Mouse (Tumor)
Probability of Survival
WT→WT
Cre-lox→WT
0.001
Days Elapsed
F.
WBCs
0.0206
Monocytes
0.0029
RBCs
0.0029
Hb
0.0088
HCT
0.0074
K/uL
g/dL
%HCT
WT→WT
Crelox→WT
G.
Bone Marrow
WT
6.62
KRAS G12D+
92.2
Ter119+
0.0005
CD34+
0.0017
%BMCs
H.
PBMCs
WT
0.72
KRAS G12D+
98.9
CD34+
0.0009
%PBMCs
I.
Thymus
WT
8.90
KRAS G12D+
79.4
CD34+
0.0012
%Thymocytes
J.
Spleen
WT
14.6
KRAS G12D+
82.0
Ter119+
0.0001
CD34+
0.0002
%Splenocytes
K.
Spleen Weight/ Body weight (%)
0.0029
Liver Weight/ Body weight (%)
0.0029
Thymus Weight/ Body weight (%)
0.0206
L.
Bone Marrow
Liver
Spleen
Thymus
Kidney
Salivary Glands
Pancreas
WT→WT
Cre-lox→WT
M.
Primary Engrafted
Mouse
Secondary
Engraftment
Secondary Engraftment
WT
76.5
KRAS G12D+
10.0
Ter119
0.001
CD83 MFI
0.001

Figure 6: Establishing the transplantable *Kras*^{G12D} *in vivo* model.

A. Experimental design of creating the *Kras*^{G12D} mouse model. Schematic created in Biorender.com.

B. Representative Hematoxylin and Eosin images from spleen, liver, and thymic tissues from primary engrafted mice at two and four months post-transplant (Scale bar= 50 um). No microscopic findings in the thymus were observed at 2 months.

C. Representative flow cytometric analysis of tumor in a 4-month old primary engrafted mouse 4 months post-transplant. CD11b and CD34 analysis done within the *Kras*^{G12D} cell population.

D. Representative flow cytometric analysis of bone marrow aspirates of primary engrafted mice, 7 weeks after transplant of Ad5CMVCre-infected c-kit^{+} Rosa26-LSL-tdTomato+/Kras-LSL-G12D bone marrow cells (left panel, quantification shown in Supplementary Fig. 7B). Bar plots showing percentage of Ter119^{+} and CD11b^{+} BMCs in *Kras*^{WT} or *Kras*^{G12D} mice (middle and right panels, respectively; n = 4 mice, P-values from Wilcoxon matched pairs t-test).

E. Experimental design of transplant study using bone marrow from WT mice or *Kras*^{G12D} mice (abbreviated as Cre-lox) with a tumor (left panel). Schematic created in Biorender.com. Kaplan Meir survival curve of both transplanted conditions.

F. White blood cells (WBC), Monocytes, Red blood cells (RBCs), Hemoglobin (Hb), Hematocrit (HCT) readings from CBC machine; n= 14 mice, P-values from Mann Whitney.

G. Representative flow cytometric analysis of bone marrow cells (BMCs) at terminal time point. Bar plots showing percentage of Ter119^{+} and CD34^{+} within live *Kras*^{WT} or *Kras*^{G12D} compartment; n= 14 mice, P-values from Wilcoxon t-test.

H. Representative flow cytometric analysis of peripheral blood mononuclear cells (PBMCs) at terminal time point. Bar plots showing percentage of CD34^{+} within live *Kras*^{WT} or *Kras*^{G12D} compartment; n= 14 mice, P-values from Wilcoxon t-test.

I. Representative flow cytometric analysis of thymus at terminal time point. Bar plots showing percentage of CD34^{+} within live *Kras*^{WT} or *Kras*^{G12D} compartment; n= 14 mice, P-values from Wilcoxon t-test.

J. Representative flow cytometric analysis of spleen at terminal time point. Bar plots showing percentage of CD34^{+} within live *Kras*^{WT} or *Kras*^{G12D} compartment; n= 14 mice, P-values from Wilcoxon t-test.

K. Normalized weights of spleen, liver, and thymus tissues from Cre-lox or WT transplanted mice at experiment termination; n = 14 mice, P-values from Mann Whitney.

L. Representative Hematoxylin and Eosin images of affected tissues from secondary engrafted mice after a month of treatment. Bar scale = 50um.

M. Experimental design of bone marrow from primary *Kras*^{G12D} mice without tumors (left panel). Schematic created in Biorender.com. Representative flow cytometry analysis of bone marrow aspirates of secondary engrafted mice after 5.5 weeks post-transplant. (left panel, quantification shown in Supplementary Fig. 7F). Bar plot showing percentage of Ter119+ BMCs and CD83 Median Fluorescent Intensity (MFI) in live *Kras*^{WT} or *Kras*^{G12D} cells (right panel, n = 11 mice. P-value from Wilcoxon matched pairs t-test).

Figure 7

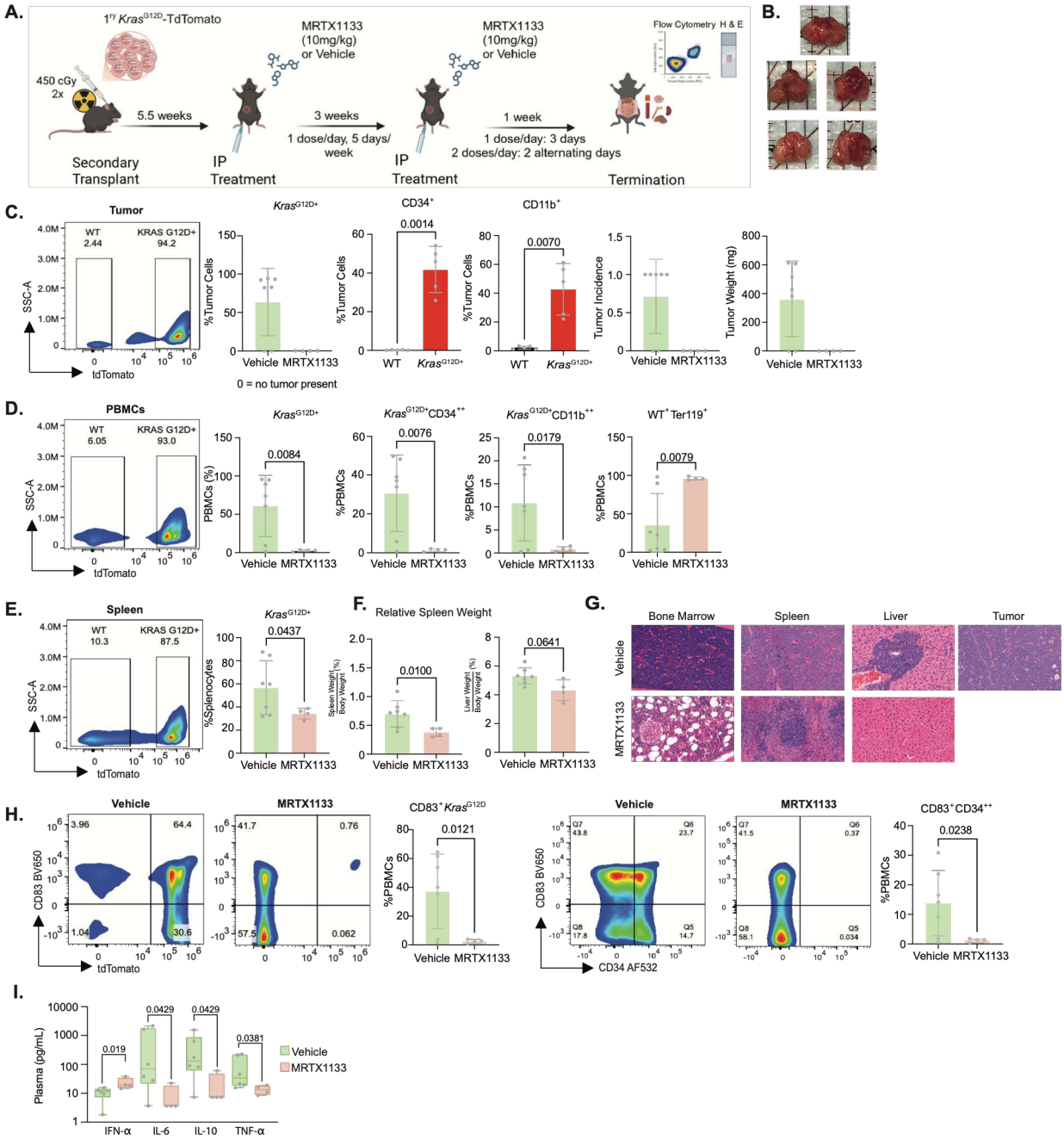


Figure 7: MRTX1133 treatment significantly reduces circulating *Kras* mutant cells, extramedullary hematopoiesis, and myeloid sarcoma formation in secondary engrafted mice.

A. Experimental design scheme of secondary transplanted *Kras*^{G12D} mice treated with MRTX1133 or not (created in biorender.com).

B. Images of five tumors extracted from seven vehicle-treated mice, with no tumors observed in MRTX1133-treated mice at experimental termination.
C. Representative flow cytometry of tumor samples showing percentage of live *Kras*^{WT} and *Kras*^{G12D} cells at experiment termination panel). Bar plots showing percentage of *Kras*$^{G12D+}$ tumor cells in vehicle treated mice, percentage of CD34^{+} cells in *Kras*^{WT} versus *Kras*$^{G12D+}$ tumor cells, and percentage of CD11b^{+} cells in *Kras*^{WT} versus *Kras*$^{G12D+}$ tumor cells; n= 11 mice, P-values from paired t-test. (**C1:** 4 left-most panels**).** Graphical representation of tumor burden at experimental termination, 1 indicating presence of tumor and 0 absence of tumor and bar plot of tumor weight (**C2:** last two panels).
D. Representative flow cytometry of PBMCs showing percentage of live *Kras*^{WT} and *Kras*$^{G12D+}$ cells at experiment termination (left panel). Bar plots showing showing percentage of *KRAS*$^{G12D+}$ PBMCs of MRTX11333 and vehicle treated mice, percentage of CD34+ cells in WT KRAS versus *Kras*$^{G12D+}$ PBMCs, percentage of CD11b^{+} cells in *Kras*^{WT} versus *Kras*$^{G12D+}$ PBMCs, percentage of Ter119^{+} cells in *Kras*^{WT} versus *Kras*$^{G12D+}$ PBMCs; n= 11 mice, P-values from paired t-test.
E. Representative flow cytometry of cells from spleen showing percentage of *Kras*$^{G12D+}$ cells at experiment termination (left panel). Bar plots showing percentage of live *Kras*^{WT} and *Kras*$^{G12D+}$ splenocytes of MRTX11333 and vehicle treated mice; n = 11 mice, P-values from paired t-test.
F. Normalized weights of spleen and liver tissues from MRTX1133- or vehicle-treated mice at experiment termination; n = 11 mice, P-values from paired t-test.
G. Hematoxylin and eosin staining of different tissues from secondary engrafted mice after a month of treatment. Images at 40x magnification.
H. Representative flow cytometry of PBMCs showing percentage of CD83^{+} and tdTomato *Kras*$^{G12D+}$ cells (left). Bar plots showing percentage of live CD83^{+}*Kras*$^{G12D++}$ PBMCs in MRTX1133 versus vehicle treated mice tumor cells. Representative flow cytometry of PBMCs showing percentage of live CD83^{+} and CD34^{+} cells (right) in MRTX1133 versus vehicle treated mice tumor cells. Bar plots showing percentage of live CD83^{+}CD34^{++} PBMCs in MRTX1133 versus vehicle treated mice tumor cells; n= 11 mice, P-values from Welch's t-test.
I. Peripheral IFN-α, IL-6, IL-10, and TNF-α levels as determined by luminex in MRTX1133 versus vehicle treated mice; n= 11 mice. P-values from Mann Whitney.

Figure 8

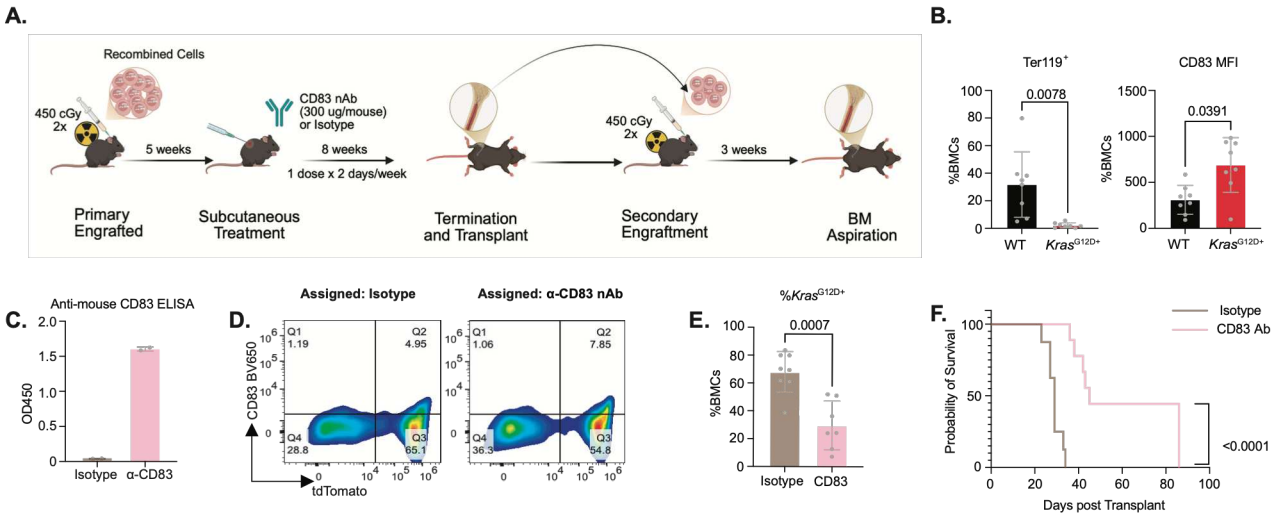


Figure 8: CD83 promotes leukemogenesis *in vivo*.

A. Experimental design scheme of primary transplanted *Kras*^{G12D} mice treated with CD83 neutralizing antibody (nAb) or isotype control and then secondarily transplanted into recipient mice (created in biorender.com).

B. Bar plots showing percentage of live Ter119^{+} cells (left) or CD83 Median Flourescent Intensity (MFI, right) in *Kras*^{WT} and *Kras*^{G12D} BMCS ; n=8. P value from Wilcoxon t-test.

C. Anti-CD83 ELISA showing binding of anti-mouse CD83 neutralizing antibody (nAb) to mouse CD83 ligand.

D. Representative flow cytometry of live CD83^{+} and tdTomato (*Kras*^{G12D}) BMCs at bone marrow aspiration; n=2. After BM flow cytometry, each plot represents a mouse that was assigned to an antibody treatment.

E. Bar plots showing percentage of live *Kras*$^{G12D+}$ BMCs of secondarily transplanted mice; n=15. P value from Welch's t-test.

F. Survival graph of 8A-8E; n=15. P value from Mantel Cox test.

SUPPLEMENTARY FIGURE LEGENDS

Supplementary Figure 1 (related to Figure 1). Single-cell profiling of cells from clonal hematopoiesis sample

A. Box plots showing number of UMIs (left panel) and genes (right panel) detected per cell after filtering based on quality control (QC) metrics (**methods**).

B. Bar plot showing percentage of *KRAS* G12D-mutant or wildtype cells from specific cell types.

C. Volcano plot showing genes differentially expressed (DE) between *KRAS* G12D-MUT and WT erythrocytes via logistic regression model (**methods**). Highlighted in green are chromatin remodelers, in purple DNA repair genes, in orange cell cycle genes and in blue interferon response genes. Adjusted p-values correspond to p-values corrected for multiple testing via Benjamini-Hochberg adjustment.

D. Downregulation of interferon gamma response and upregulation of cell cycle highlighted by pre-ranked gene set enrichment analysis (GSEA) using the MSigDB Hallmark collection (hypergeometric test, **methods**). NES corresponds to the normalized enrichment score from the pre-ranked GSEA. Genes DE between *KRAS* G12D-mutant and wildtype erythrocytes as in **Supplementary Fig. 1C**. Only significantly enriched pathways shown (Benjamini-Hochberg adjusted p-value < 0.05).

E. Violin plot showing *KRAS* expression in erythrocytes and monocytes. P-value from Wilcoxon rank sum test, *: p-value < 0.05.

Supplementary Figure 2 (related to Figure 2). Single-cell profiling of cells from AML samples

A. Box plots showing number of UMIs (left panel) and genes (right panel) detected per cell in each AML sample, after filtering based on quality control (QC) metrics (**methods**).

B. Uniform Manifold Approximation and Projection (UMAP) of cells from AML1 (top panel) and AML2 (bottom panel) samples overlaid with cell type assignment. Eryth: erythrocytes, AML-Lymph: AML cells with lymphoid differentiation, AML-Mono: AML cells with myeloid differentiation.

C. Dot plot showing expression levels of cell type specific gene markers in each cell group (left panel). Bar plot showing number of cells per cell group (right panel).

D. Violin plot showing expression of inflammatory genes in AML cells compared to all other cells from all samples. P-value from linear mixed model (LMM) with/without cell group label, *: p-value < 0.05.

E. Violin plot showing expression of leukemic markers in AML subgroups across all samples. P-value from Wilcoxon rank sum test comparing expression in AML-GrpB cells to all other AML cells, *: p-value < 0.05.

Supplementary Figure 3 (related to Figure 2). Comparing *KRAS*^{G12D} mutated and wild-type cells from AML samples

A. UMAP of cells from AML1 sample overlaid with *KRAS* mutational status.
B. UMAP of cells from AML2 sample overlaid with *KRAS* mutational status for G12D (left), G12V (middle) and either one (right) mutations.
C. Bar plot showing proportion of *KRAS* G12D/V mutant or wildtype cells in each patient sample. Cell numbers are highlighted within each bar in white.
D. Bar plot showing proportion of *KRAS* G12D/V mutant or wildtype cells across each cell type per sample. Cell numbers are highlighted within each bar in white.
E. Heatmap showing expression of inflammatory genes in *KRAS* G12D/V-mutant AML cells. P-values from Wilcoxon rank sum test, *: p-value < 0.05.
F. Heatmap showing cell cycle module scores in KRAS G12D/V-mutant AML cells. Cell cycle genes from Tirosh et al 2016(87). P-values from Wilcoxon rank sum test, *: p-value < 0.05.

Supplementary Figure 4 (related to Figure 3)
A. Box plots showing CD83 expression in each sorted cell population per AML subgroup. P-values from Wilcoxon rank sum test. LT-HSC, Long-Term Hematopoeitic Stem Cells (HSC); ST-HSC, Short-Term HSC; GMP, Granulocyte-monocyte progenitors. P-values from Wilcoxon rank sum test.
B. Gating strategy for sorting $DAPI^{-}CD45^{+}CD83^{+}$ single cells, based on CD83 FMO control.
C. Bar plot showing percentage of live $CD34^{+}$ cells in each sorted or unsorted cell condition (continuation of **Fig. 3C**). Cell percentage from flow cytometry (n = 3 biological replicates). P-values from paired one-tail t-test.
D. Representative images of erythroid and myeloid colonies in each condition from clonogenic assays (left panel). Bar plot showing the quantification of the colonies in each condition (right panel). n = 2-3 experiments, P-values from paired one-tail t-test.

Supplementary Figure 5 (related to Figure 4). **Single-cell profiling of cells from CH1 patient treated or not with MRTX1133.**
A. Box plots showing number of UMIs (left panel) and genes (right panel) detected per cell in each AML sample, after filtering based on quality control (QC) metrics (**methods**).
B. Dot plot showing expression levels of cell type specific gene markers in each cell group (right panel). Bar plot showing number of cells per cell group (left panel).
C. Bar plot showing proportion of *KRAS* G12D/V mutant or wildtype cells across each cell type per sample. Cell numbers are highlighted within each bar in white.

Supplementary Figure 6 (related to Figure 5). KRAS G12D inhibition across primary patient samples and healthy controls.
A. Representative flow cytometry response of cells from AML4, MDS1, and CH1 patients to increasing doses of MRTX1133. Cumulative colony assay neutrophil flow data on MDS1 (n=3 biological replicates, right panel) and CH1 cells (n=5 biological replicates, right panel) treated with DMSO or 500 nM MRTX1133. P value from LMM test.

B. Flow analysis of MDS1 PBMCs treated with DMSO or 500 nM MRTX1133. Erythroid population is gated on CD45 negativity (n=3 biological replicates, left panel). Number of erythroid colonies in MDS1 treated cells (n=3 biological replicates, right panel). P value from LMM test.
C. PBMCs from healthy individuals treated with DMSO or 500 nM MRTX1133. Erythroid population is gated on CD45 negativity while myeloid cells are gated by CD45 positivity(n=3 biological replicates).
D. Bar plot showing number of erythroid or monomyelocytic colonies from PBMCs from healthy individuals treated with vehicle or 500 nM MRTX1133. Normalized counts represent MRTX1133 treated counts normalized to that of DMSO-treated cells.

Supplementary Figure 7 (related to Figure 6). Generation and validation of the KRAS G12D *in vivo* model.
A. Gel images showing Kras G12D-Lox-Stop-Lox (LSL, left panel) and tdTomato (right panel) genotyping results. Expected wildtype (WT) LSL band is 880 bp and Kras G12D LSL cassette band is 491 bp. On tdTomato gel, WT band is 297 bp and tdTomato band is 196 bp. Negative control is denoted by - while positive control is denoted by +. Mouse chosen (denoted by *) is *Kras* G12D $LSL^{+/-}$ and $tdTomato^{+/-}$. This donor refers to Fig 6A-6D and 6M.
B. Necropsy of a primary engrafted mouse that died 4 months after transplant.
C. Bar plot showing percentage of $Kras^{WT}$ or $Kras^{G12D+}$ BMCs from bone marrow aspirates of primary transplanted mice, 7 weeks after transplant (left panel). Flow cytometry analysis, n = 4 mice, P-value from unpaired t-test. Gating strategy for assessing proportion of Ter119+ and $CD11b^{+}$ cells in the *Kras* WT and Mutant compartment (quantification in **Fig. 6D**).
D. Gel images showing Kras G12D-Lox-Stop-Lox (LSL, left panel) and tdTomato (right panel) genotyping results. The starred donor refers to Fig 6E-6L.
E. Necropsy of an irradiated WT donor (left) and corresponding hematoxylin and eosin stained liver tissues (right). This donor refers to Fig 6E-6F, and 6K.
F. Necropsy of an irradiated primary AdenoCreLox engrafted donor (left) and corresponding hematoxylin and eosin stained liver tissues (right). This donor refers to Fig 6E-6L.

Supplementary Figure 8 (related to Figure 6). Generation and validation of the KRAS G12D *in vivo* model.
A. Mean Corpuscular Volume (MCV), Reticulocytes (Retics), Platelets (PLT), Lymphocytes, Neutrophils, Basophils, Red Cell Distribution Width (RDW), Plateletcrit (PCT), Platelet Distribution Width (PDW), and other measurements are reported using standard clinical units (top: pg, fL K/uL, bottom: %) according to the CBC analyzer output (n= 14 mice, P-values from Mann Whitney).
B. Representative Hematoxylin and Eosin stained sections of tissues from secondary engrafted mice transplanted with WT cells (left) or primary AdenoCreLox cells (right).
C. Representative flow cytometry gating of BM cells from secondary engrafted Crelox mice (quantification in **Fig 6G**.)

D. Bar plot showing percentage of *Kras*^{WT} or *Kras*$^{G12D+}$ BMCs from bone marrow aspirates of secondary transplanted mice, 5.5 weeks after transplant (left panel). Flow cytometry analysis, n = 11 mice, P-value from unpaired t-test. Gating strategy for assessing proportion of Ter119^{+} and CD11b^{+} cells in the *Kras*^{WT} or *Kras*$^{G12D+}$ compartment (quantification in **Fig. 6E**).

Supplementary Figure 9 (related to Figure 7) MRTX1133 relieves the erythroid differentiation block.
A. Bar plots showing percentage of CD11b^{+}GR-1^{++} PBMCs and percentage of CD14^{+} PBMCs from secondarily engrafted mice tissues after 1 month of treatment. All cell percentage assessed by flow cytometry data; n = 11 mice, P-values from paired t-test.
B. Left bar plot shows percentage of Ter119^{+} cells in *Kras*^{WT} or *Kras*$^{G12D+}$ tumor cells of vehicle treated mice. Right bar plot shows percentage of Ter119^{+} PBMCs in *Kras*^{WT} or *Kras*$^{G12D+}$ cells in MRTX1133 and vehicle treated mice. All cell percentage assessed by flow cytometry data; n = 11 mice, P-values from paired t-test.

Supplementary Figure 10 (related to Figure 8). Antibody mediated anti-CD83 blockade *in vivo*.
A. Gel images showing Kras G12D-Lox-Stop-Lox (LSL, left panel) and tdTomato (right panel) genotyping results. Expected wildtype (WT) LSL band is 880 bp and Kras G12D LSL cassette band is 491 bp. On tdTomato gel, WT band is 297 bp and tdTomato band is 196 bp. Negative control is denoted by - while mouse chosen (denoted by *) is Kras G12D LSL+/- and tdTomato+/. This donor refers to Fig 8A-8E and 6M.
B. Bar plot showing live *Kras*^{WT} or *Kras*$^{G12D+}$ BMCs assessed by flow cytometry (referring to Fig 8B).
C. Proposed model for *Kras*^{G12D} role and its specific inhibition in myeloid neoplasms observed in patients and our transplantable mouse model.

SUPPLEMENTARY TABLES

Supplementary Table 1 (related to Figures 1, 2 and 4). Clinical and mutational information for all primary samples profiled.
Supplementary Table 2 (related to Figure 1). Transcriptional differences between *KRAS*-G12D mutant and wildtype erythrocytes from clonal hematopoiesis patient. Deregulated genes and pathways are provided.
Supplementary Table 3 (related to Figure 2). Transcriptional differences between *KRAS*-G12D mutant and wildtype AML cells. Deregulated genes and pathways are provided.
Supplementary Table 4 (related to Figure 4). Transcriptional differences between *KRAS*-G12D mutant MRTX1133-treated versus untreated GMP cells from clonal hematopoiesis patient. Deregulated genes and pathways are provided.
Supplementary Table 5 (related to methods). List of primers and antibodies.

Supplementary Table 6 (related to methods). Hematoxylin and eosin staining protocol
Supplementary Table 7 (related to Fig 7). Raw Luminex data and dilution information

Supplementary Files

This is a list of supplementary files associated with this preprint. Click to download.

- SupplementaryTable6.xlsx
- SupplementaryTable4.xlsx
- SupplementaryTable1.xlsx
- SupplementaryTable2.xlsx
- SupplementaryTable3.xlsx
- SupplementaryTable7.xlsx
- SupplementaryTable5.xlsx